J. Fluid Mech. (2022), *vol.* 933, A39, doi:10.1017/jfm.2021.1043

JFM PAPERS

Topological description of near-wall flows around a surface-mounted square cylinder at high Reynolds numbers

Yong Cao[1,2,3,†], Tetsuro Tamura[3], Dai Zhou[1,2,†], Yan Bao[1] and Zhaolong Han[1]

[1]School of Naval Architecture, Ocean and Civil Engineering, Shanghai Jiao Tong University, Shanghai 200240, PR China

[2]State Key Laboratory of Ocean Engng, Shanghai Jiao Tong University, Shanghai 200240, PR China

[3]Department of Architecture and Building Engineering, Tokyo Institute of Technology, Yokohama 226-8502, Japan

(Received 2 February 2021; revised 5 November 2021; accepted 21 November 2021)

This study topologically describes near-wall flows around a surface-mounted cylinder at a high Reynolds number (*Re*) of 5×10^4 and in a very thick boundary layer, which were partially measured or technically approximated from the literature. For complete and rational flow construction, we use high-resolution simulations and critical-point theory. The large-scale near-wake vortex is composed of two connected segments rolled up from the sides of the cylinder and from the free end. Another large-scale side vortex clearly roots on two notable foci on the lower side wall. In the junction region, the side vortex moves upwards with a curved trajectory, which induces the formation of nodes on the ground surface. In the free-end region, the side vortex is compressed, which results in a smaller trailing-edge vortex and its downstream movement. Only tip vortices are observed in the far wake. The origin of the tip vortices and their distinction from the near-wake vortex are discussed. Further analyses suggest that *Re* independence should be treated with high caution when *Re* increases from 500 to $O(10^4)$. The occurrence of upwash flow behind the cylinder strongly depends on the increase in *Re*, the mechanism of which is also provided. The separation–reattachment process in the junction region and the trailing-edge vortices are discovered only at a high *Re*. The former should significantly affect the strength of the side vortex in the junction region and the latter should cause a sharp drop in pressure near the trailing edge.

Key words: separated flows, turbulence simulation, free shear layers

† Email addresses for correspondence: yongcao@sjtu.edu.cn, zhoudai@sjtu.edu.cn

1. Introduction

Surface-mounted square cylinders with a finite height immersed in a thick turbulent boundary layer are commonly encountered in engineering applications. Compared with cylinders with infinite lengths, their aerodynamic characteristics possess salient three-dimensional (3-D) effects along the vertical direction under the effects of the ground surface and free end.

1.1. *Critical flow features far from the body*

The critical flow features that are distinct from those of an infinite-length cylinder first manifest themselves in a time-averaged field. The mean flow features that are relatively far from the finite-height cylinder include the horseshoe vortex system, recirculation region around the cylinder, downwash along the centreline of the wake, upwash behind the cylinder–plane junction, tip vortex pair originating from the free end and base vortex pair in the lower half of the wake near the ground surface. The mean or dynamic flow structures in the wake have been extensively investigated through experiments in studies by Sakamoto & Arie (1983), Okuda & Taniike (1993), Wang & Zhou (2009), Bourgeois, Sattari & Martinuzzi (2011), Kawai, Okuda & Ohashi (2012), Porteous, Moreau & Doolan (2016), Sumner *et al.* (2017), Unnikrishnan, Ogunremi & Sumner (2017), Zhang *et al.* (2017), Rastan, Sohankar & Alam (2017), Sohankar *et al.* (2018), Yauwenas *et al.* (2019) and Wang, Thompson & Hu (2019). A thorough understanding of the vortex-shedding wake has been achieved, although it is affected by many external factors, such as the Reynolds numbers ($Re = UD/\nu$, where U is the characteristic velocity, D is the characteristic width of the cylinder and ν is the kinematic viscosity), approaching boundary layer, aspect ratio ($AR = H/D$, where H is the height of the cylinder) and sharpness of the cylinder edges.

From a time-averaged perspective, the wake structures generally include dipole and quadrupole types, which are characterised by two and four patches of alternating senses of rotation, respectively. The two patches in the upper part of the wake (i.e. pair of tip vortices) are induced by the downwash flow from the free end and always occur relatively independently of the flow conditions. Kawamura *et al.* (1984) were one of the first groups to illustrate the appearance of a pair of longitudinal tip vortices (trailing vortices) in the case of a finite-height circular cylinder. In comparison, the two patches in the lower part of the wake (i.e. pair of base vortices) were associated with the upwash flow from the ground surface. Their occurrence was not necessarily observed in every study and was determined to be strongly influenced by the relative thickness of the boundary layer, aspect ratio and Re (Wang *et al.* 2006; Hosseini, Bourgeois & Martinuzzi 2013; Rastan *et al.* 2017; Sumner *et al.* 2017; Zhang *et al.* 2017; Behera & Saha 2019; Yauwenas *et al.* 2019). A thicker boundary layer tends to produce base vortices (Wang *et al.* 2006; Hosseini *et al.* 2013) and the quadrupole wake model is the result. Conversely, base vortices are absent (corresponding to the dipole wake model) in a thinner boundary layer. The 'six-vortex type' was also observed by Zhang *et al.* (2017) at $Re = 150$ and 250, and Rastan *et al.* (2017) at $Re = 100$ and 150, although the aspect ratio and Re differed between the two studies. Rastan *et al.* (2017) and Rastan *et al.* (2019) reported that the structure of the 'multipolar-wake' or 'six-vortex' types is the transition of the mean vortex structure from the dipole to the quadrupole type.

The first widely accepted vortex-shedding model may be the arch and Kármán types (Sakamoto & Arie 1983), which were found to appear when the aspect ratios were lower and higher than the critical aspect ratio, respectively. However, this shedding model does not satisfactorily explain the formation of the streamwise tip and base vortices and their interactions with the instantaneous flow structures (da Silva *et al.* 2020).

Wang & Zhou (2009) extended the arch-type vortex to the 3-D vortex structure, which may explain the connection of the vortex structure with the streamwise tip and base vortices. The proposed arch-type vortex has two spanwise vortices from both sides of the cylinder, which connect near the free end. Both the upper and lower parts of the arch-type structure are inclined upstream under the influence of the free-end downwash flow and the boundary layer over the ground surface. The tip and base vortices are attributed to the streamwise projection of the arch-type vortex. Symmetric and asymmetric modes are instantaneously observed, with asymmetric staggered spanwise vortices more likely to occur in the middle-height region. Bourgeois *et al.* (2011) and Hosseini *et al.* (2013) employed particle image velocimetry (PIV) and phase averaging techniques to clarify the shedding modes behind a surface-mounted square cylinder. Half- and full-loop vortical structures were proposed for dipole and quadrupole wakes behind the cylinder in thin and thick boundary layers, respectively. The half-loop structure consists of a principal core, which is nearly vertical at the ground surface, and the connector strand, which connects the bottom of the principal core to the top of the downstream principal core. The dynamic wake when $AR = 4$ and in a thin boundary layer (Bourgeois *et al.* 2011) is characterised by alternating shedding of half-loop structures. The tip vortex in the mean field can be easily understood as a footprint of the connector strand in the free-end region. The shedding of half-loop structures was confirmed by direct numerical simulation (DNS) by Saeedi, Lepoudre & Wang (2014). In the quadrupole wake, both ends of the principal core bend towards the cylinder. The full-loop structure is formed by the principal core and two connector strands in the free-end and junction regions. Thus, the streamwise tip and base vortices observed in the quadrupole wake are thought to be the time-averaged footprints of the top and bottom connector strands. However, a lack of agreement remains regarding the origin of the streamwise tip and base vortices and their relation with the near-wake vortex structures (da Silva *et al.* 2020; Rastan *et al.* 2021). da Silva *et al.* (2020) conducted time-averaged flow analysis for a square cylinder with $AR = 3$ and $Re = 500$ based on a numerical simulation. The downwash directly attached to the ground surface and the base vortices were found to be absent; only the tip vortex was present. The origin of the tip vortex was attributed to the 3-D bending of the side flow by the downwash, which is inherently distinct from the previous mechanisms. Rastan *et al.* (2021) further investigated the origin of the tip vortex (with the absence of a base vortex) behind a square cylinder when $AR = 7$ and $Re = 1.2 \times 10^4$ and suggested that it originates from the roll-up of the flow from the side face to the top (called the 'primary tip vortex' in their study). In addition to the tip vortices, no consensus exists regarding the formation and development of the base vortex, even though base vortices are normally regarded as being strongly associated with the upwash in the junction region. Bourgeois *et al.* (2011), Sumner *et al.* (2017) and Kawai *et al.* (2012) observed the upwash flow in the symmetry plane when $AR = 2.7$–5 and $Re = O(10^4)$ despite the relative weakness in the magnitude. In contrast, the upwash was not found by da Silva *et al.* (2020) at a much lower Re of 500. Interestingly, the absence of the base vortices was claimed in these studies, which suggests that the upwash does not necessarily result in base vortices. In addition, the effects of the Re in the range of 500 to $O(10^4)$ seem unclear in terms of the upwash flow in the junction region, considering Re ranges of <50 and <1000 were systematically investigated by Rastan *et al.* (2017) and Zhang *et al.* (2017).

1.2. *Near-wall flow patterns*

In contrast to the extensive studies of flow/vortices far from the cylinder, quantitative data on near-wall flow patterns have rarely been observed, possibly owing to technical difficulties, regardless of time-averaged or dynamic patterns. The near-wall flows are critical for skin friction, pressure on the walls of the cylinder, and heat transfer between the body and flow. Surface oil flow visualisation (extensively applied by Martinuzzi & Tropea 1993 and Sumner 2013) typically cannot supply the precise locations of critical points, as suggested by Tian, Simpson & Tang (2004) and Depardon *et al.* (2005). Gravity prevails over shear friction for pigments on the lateral side walls of the body, which drags the pigment downwards and increases the difficulty of distinguishing critical points. Castro & Dianat (1983) and Depardon *et al.* (2005) quantitatively measured the skin-friction patterns on the walls of a surface-mounted rectangular body and cube using pulsed wall gauges and a near-wall PIV technique, respectively. Recently, near-wall PIV visualisation was extended to the area above the free end of a finite square cylinder (Sumner *et al.* 2017). However, complete surface flow patterns on square cylinders of finite height by oil flow visualisation or near-wall PIV techniques are lacking.

Instead, numerical simulations provide a more reasonable means of systematically investigating the flow patterns very near the walls of the cylinder. Therefore, recent years have witnessed an outpouring of near-wall flow investigations using high-accuracy numerical simulations. However, most numerical simulations have been conducted in the range of low Re values of 40–1000 (Saha 2013; Rastan *et al.* 2017; Zhang *et al.* 2017; Behera & Saha 2019; da Silva *et al.* 2020). Both Rastan *et al.* (2017) and Zhang *et al.* (2017) indicated variations in near-wall flows under the effects of different Re values. At $Re = 40$ or 50, no backflow region (i.e. no separation) could be observed on the side wall of the cylinder or on the top wall. When the Re was greater than 100, separation occurred, and two foci formed on the top wall of the cylinder. The distance between the two foci increased with an increase in Re up to 1000. On the rear wall, the skin friction lines originated from an attachment point. Upward and downward flows were clearly identified by the attachment point on the rear wall. On the side wall, a (partially) quasi-horizontal dividing line could be identified, above and below which the mean streamlines turned upwards/downwards (Rastan *et al.* 2017; Zhang *et al.* 2017), although the dividing line passed through the lower corner at the highest Re (i.e. 1000) tested by Zhang *et al.* (2017). These features were verified again by da Silva *et al.* (2020) when $Re = 500$. da Silva *et al.* (2020) further investigated the surface-flow patterns and vortices around the cylinder. The connection of the surface flow pattern, flow separation and vortices around the cylinder were established based on a detailed visualisation of the low-Re flow simulations.

Considering the lack of near-wall flow patterns, particularly for high-Re flows, our previous work (Cao, Tamura & Kawai 2019) offers a database of near-wall flows visualised by skin-friction lines on the walls based on very high-resolution numerical simulations when Re was 5×10^4. The visualisation indicated a noticeable difference in the near-wall flow pattern between the low- and high-Re flows. Considering the wider application in practice of high Re, the near-wall flow patterns at high Re and their variations arising from an increase in Re must be explored. This study further clarifies the relationship between the surface flow patterns and outer separated flow (or vortices). A skeleton of 3-D flow separation is proposed in this study.

1.3. *Methodology for near-wall flow description*

The flow patterns deduced from flow-visualisation measurements, regardless of experiments or simulations, are often incomplete and approximate in the literature. For example, Bourgeois *et al.* (2011) could not provide near-wall flow patterns even though they applied the PIV technique to propose a half-loop shed structure in the wake and Unnikrishnan *et al.* (2017) failed to measure the velocity vectors in the recirculation zone behind the cylinder using a seven-hole probe. In some cases, a relatively complete flow field was attempted using PIV or numerical simulations (Kawai *et al.* 2012; Saeedi *et al.* 2014). However, the flow topology was schematically described without any strict reasoning. Sometimes a large variation may occur in the flow pattern, inferred from similar data obtained by different investigators (Hunt *et al.* 1978). The critical-point theory is necessary to overcome these difficulties and ambiguities. The theory originates from Poincaré's work on the singularities of differential equations (Poincaré 1891) and is important for interpreting and understanding flow patterns, whether they are obtained experimentally or computationally (Perry & Chong 1987; Délery 2001). The theory can provide a convincing and rational description of a 3-D separated flow. Thus, a rational flow topology is preferable to satisfy the critical-point concept. The critical-point theory has been applied to describe high-*Re* flows around a circular or square cylinder with infinite length (Huang, Chen & Hsu 2006; Huang, Lin & Yen 2010), the low-*Re* flow around a surface-mounted cube (Liakos & Malamataris 2014, 2016) and the flow around a hemisphere-cylinder (Le Clainche *et al.* 2016). However, it is surprising that a rational and detailed flow topology is lacking with respect to the fundamental flow configuration around a surface-mounted square cylinder. Therefore, in this study, the critical-point theory is expected to be applied to high-*Re* flows around a surface-mounted square cylinder immersed in a turbulent boundary layer.

In summary, three unclear points in the literature motivate this study, despite the many attempts to describe the wake flow structures of a surface-mounted square cylinder. The first is incompleteness (partially measured or technically approximated) or irrationality (overlooking the critical-point theory) of information of near-wall flow patterns, particularly at high *Re*, often encountered in engineering applications. The second is the origin of the tip and base vortices (if they exist) and their relationship with the other structures in the wake, at least from a time-averaged perspective. The third is the effect of the *Re* on the near-wall and near-wake flow topologies in the range of $Re = 500–O(10^4)$, particularly for the upwash formation. This study aims (1) to address the obvious ambiguity of the near-wall flow patterns and their connection to the 3-D separation around the cylinder at high *Re* values; (2) to elucidate the origin and development of the tip and base vortices (if they exist) in the far wake and (3) to clarify the variations in near-wall and near-wake flow patterns in different ranges of low and high *Re* values. This study emphasises two advantageous tools for achieving these goals. First, a very high-resolution Cartesian grid is used to capture small-scale flow properties to the greatest extent possible, which is essential for capturing the variations between low- and high-*Re* flows. In addition, the critical-point theory is strictly applied to describe the flows topologically, which is regarded as the sole tool for constructing a rational and consistent flow topology (Délery 2001). The rational construction of flow topology will contribute considerably to understanding the flow organisation and validating other data sources with similar flow configurations.

2. Numerical method and validation

2.1. *Numerical method*

This study uses the code 'CUBE' developed by the Riken Centre for Computational Science (Jansson *et al.* 2019; Onishi & Tsubokura 2021). It combines the building cube method (BCM) with the topology-independent immersed boundary method (IBM). The topology-independent IBM was proposed and implemented by Onishi *et al.* (2013, 2018) under the framework of BCM (Nakahashi 2002, 2005). This method is simple in all flow simulation stages (i.e. mesh generation, solution algorithm and post-processing). Owing to space limitations, the numerical details are not repeated in this study (interested readers are referred to the aforementioned references). The incompressible continuity and Navier–Stokes equations are solved based on the Cartesian grid without any explicit subgrid-scale (SGS) modelling for turbulence. The convective and diffusion terms are spatially discretised using the second-order central difference scheme, and 5 % of the first-order upwind scheme is blended to estimate the convective flux on the cell face. The fractional-step method is applied for time marching. The semi-implicit Crank–Nicolson method is used to treat the convective and diffusion terms. The semi-implicit velocity and Poisson equations are solved using the red/black successive over-relaxation method.

The numerical process and set-up are the same as those of Cao *et al.* (2019). A model of the surface-mounted square cylinder immersed in a thick boundary layer is schematically shown in figure 1(*a*) when $Re = 5 \times 10^4$. The aspect ratio of the cylinder is $AR = 3$. The thickness of the turbulent boundary layer is $\delta/D = 20.1$. The origin of the axis is placed at the centre of the bottom of the cylinder. The computational domain size is $32D \times 8D \times 32D$ in the streamwise (x), lateral (y) and vertical (z) directions. The domain size is examined in Appendix A. The grid system in the symmetry plane is shown in figure 1(*b*). The x–y plane at the middle height of the cylinder is shown in figure 1(*c*). The minimum cell size is determined from the thickness of the boundary layer on the cylinder (δ_B). According to White (2006), $\delta_B \approx 5.5 \times (0.5D)/\sqrt{Re_{0.5D}} = 0.0174D$. In this study, the cell size in the wall-normal direction is $\varDelta = 0.00195D$, which means that the boundary layer spans approximately nine cells. In other directions near the cylinder walls, the cell size is the same as $\varDelta$ because the elemental cells are in the shape of a cube, which means that approximately 512×512 cells are distributed in an area of $1D \times 1D$ on the surface of the cylinder. This resolution is much finer than that of most numerical simulations or experimental PIV measurements previously performed, and has the advantage of capturing finer flow structures. In addition, $\varDelta$ is the smallest cell size throughout the computational domain and is considered the reference grid resolution used to describe other regions, as indicated in figures 1(*b*) and 1(*c*). The region from the ground surface to $z/D = 1$ has a cell size of $8\varDelta$ before it approaches the cylinder. A total of 460 million cells were used in this study. The sufficiency of the current cell sizes is verified in Appendix A. The results showed that the cell sizes in the regions of the shear layer and the near and moderate wakes were nearly of the same order of magnitude as the Kolmogorov length scale estimated by Tennekes & Lumley (1972). Although an examination of strict mesh independence is preferable, the use of the present mesh is necessary to ensure an affordable computational cost. Jiang & Cheng (2020) observed the quantitative variation in the separation and reattachment points around an infinite-length square cylinder at $Re = 10$–400 when refining mesh resolutions by a factor F_{mr}. The shift in critical points was less than $0.003D$ and less than $0.04D$ when F_{mr} increased from 4 to 6 and from 1 to 6, respectively. Considering the purpose of the topological description, two topology patterns are said to be topologically equivalent if they can be distorted into another by a stretching process but without tearing (Tobak & Peake 1982; Perry & Chong 1987; Délery 2001). Accordingly, in this study, the slight quantitative shift in the critical-point locations as observed by Jiang & Cheng (2020) will not significantly influence the topological description of the flow.

The time step $\Delta t^* = (\Delta t U_\infty)/D$, (where U_∞ is the free-stream velocity) is 2×10^{-4}, which results in a maximum Courant number of approximately 0.3. Statistical analysis begins after the flow becomes statistically stationary. The duration of the statistical average is approximately $200t^*$, which corresponds to approximately 20 periods of Kármán vortex shedding. The temporal convergence of statistical pressures, forces and velocity

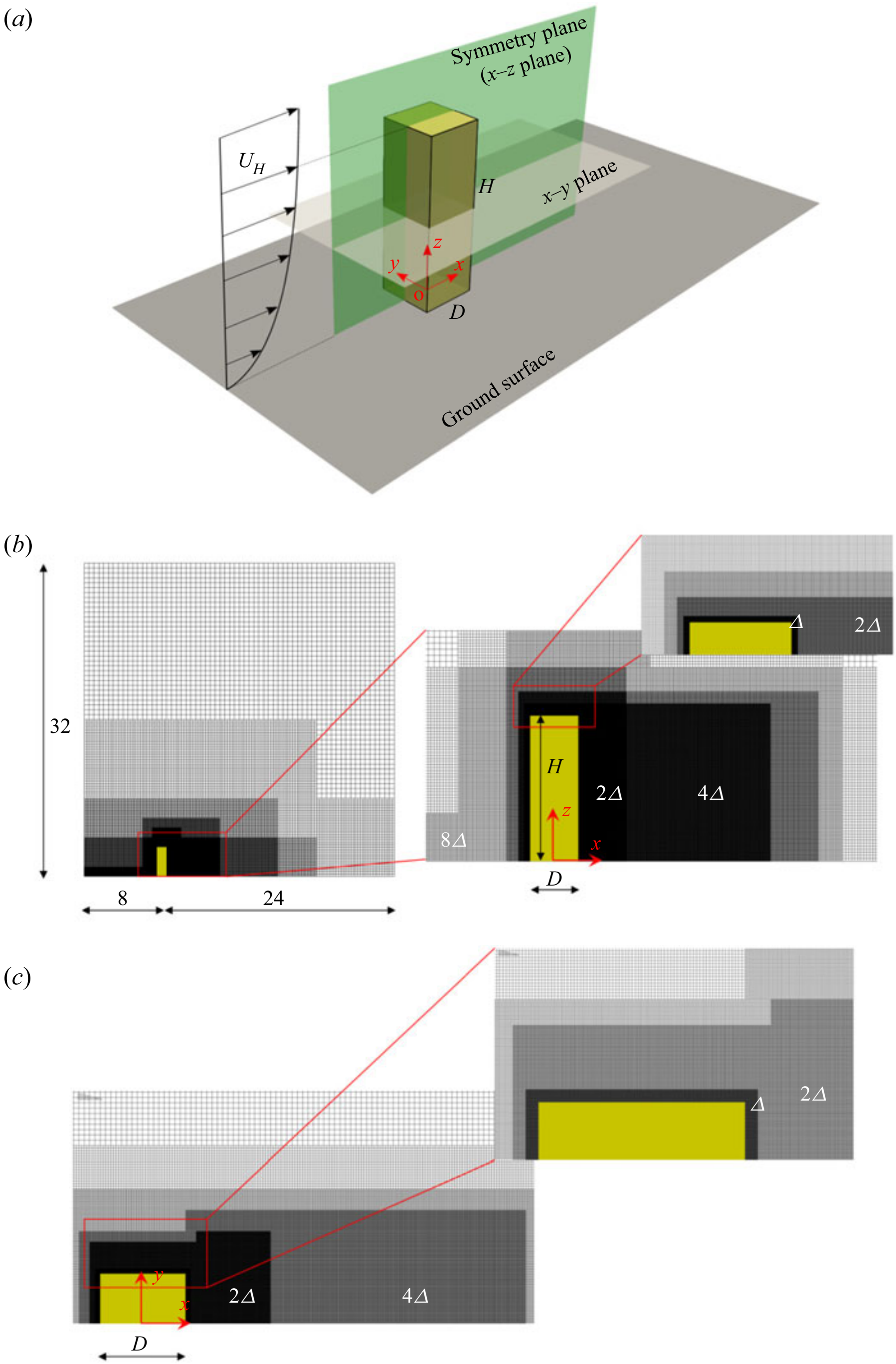

Figure 1. (a) Model of a surface-mounted square cylinder in a turbulent boundary layer when $Re = 5 \times 10^4$. (b) Grid system in the symmetry plane. (c) Grid system in the x–y plane in the middle of the cylinder. The domain sizes are normalised by D. The cell sizes are also tabbed in different regions relative to the minimum cell size Δ immediately near the immersed boundary. Panels (b) and (c) are reproduced from Cao *et al.* (2019).

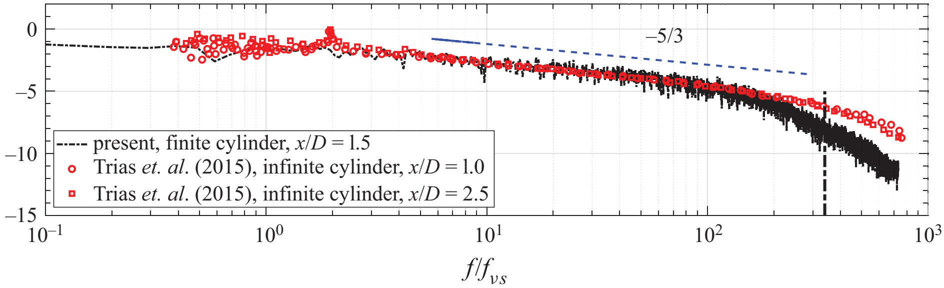

Figure 2. One-dimensional energy spectra of the streamwise velocity component in the wake. The measurement station in the present case is located at $(x/D, y/D, x/D) = (1.5, 0, 1.5)$, and those of Trias *et al.* (2015) are located along the centreline of the wake when $x/D = 1.0$ and 2.5. The vertical dash–dotted line represents the grid cut-off frequency and the blue dashed line represents a slope of $-5/3$.

is examined in Appendix B and by Cao *et al.* (2019). The computations were performed on a K-computer, one of the highest calibre supercomputers known. One computational node has a SPARC64^{TM} VIIIfx 2-GHz CPU, 128-GF performance and 16-GB memory. Each node contains eight cores. The network is based on the Tofu Interconnect (6D Mesh/Torus). In this case, 2881 computational nodes were used. The wall-clock time was approximately 7 days for 1 300 000 time steps.

The effects of small-amount numerical dissipation are examined when no explicit model is used for turbulence modelling. The energy spectra of streamwise velocity are compared in figure 2 between the present study and the DNS study by Trias, Gorobets & Oliva (2015). Note that Trias *et al.* (2015) simulated the uniform flow past an infinite-length square cylinder at a *Re* similar to that in the present case. The productivity of small-scale turbulent motion is verified by comparing the high-frequency region. In figure 2, the black vertical dashed-dotted line represents the cut-off frequency of local cells in the current study and the blue dashed line indicates the slope of $-5/3$, which indicates the inertial subrange. Clearly, the present spectrum decays earlier than in the DNS study. Furthermore, the earlier decay commences from the inertial subrange, particularly around the cut-off frequency. The present spectrum appears similar to the filtered one from the DNS results, where the filter width is approximately the cut-off wavenumber. In other words, a small numerical dissipation exists to a certain degree in time and space functions such as the SGS model, although the numerical dissipation differs fundamentally from that of the SGS model. However, the high-frequency range is reproduced sufficiently up to several hundred vortex-shedding frequencies (f_{vs}). The absence of the peak of vortex-shedding frequency ($St = f_{vs}D/U_H = 0.094$) in the streamwise velocity spectra in the centreline of the wake is similar to the phenomenon in which the peak is much less pronounced in the streamwise velocity than that in the lateral velocity in the wake centreline of bluff bodies (Ong & Wallace 1996; Parnaudeau *et al.* 2008; Cao & Tamura 2015). If the probe point is far from the cylinder in the lateral direction, the vortex shedding frequency can be observed clearly (Mcclean & Sumner 2014; Rastan *et al.* 2021).

2.2. *Numerical validation*

The inflow conditions were first examined by comparing the numerical results with the experimental results by Katsumura (as cited by Maruyama *et al.* 2013). In this study, the Lund method (Lund, Wu & Squires 1998) was used to generate a fully developed turbulent boundary layer (TBL) on a smooth ground plane. The Lund method was implemented

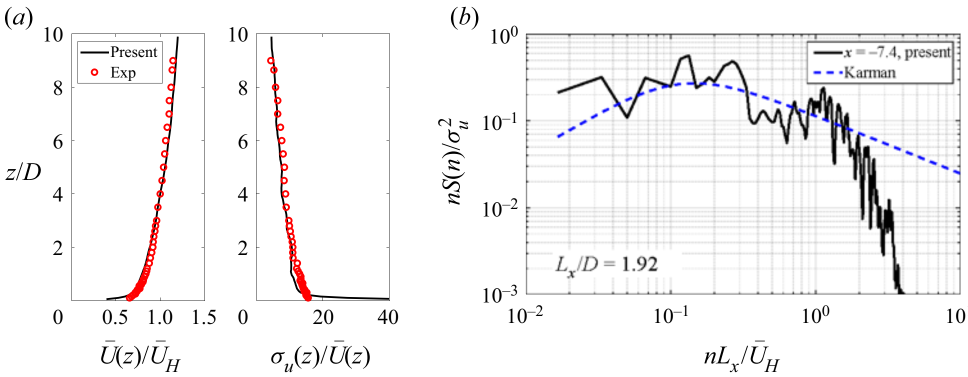

Figure 3. (*a*) Time-averaged velocity and turbulence intensity profiles near the inlet as compared with the experiment by Katsumura (Maruyama *et al.* 2013). (*b*) Power spectrum density at $(x/D, y/D, z/D) = (-7.4, 0, 4)$, where the cell size at this position is approximately $0.03D$. The figures are reproduced from Cao *et al.* (2019).

in another in-house code based on the finite difference method. The non-dimensional Navier–Stokes equations were solved, where the friction velocity and boundary-layer thickness were the characteristic velocity and length, respectively. The sampled TBL data were scaled to fit the desired TBL thickness, which imitates the atmospheric boundary layer approaching buildings. They were then input into the main domain with a finite-height square cylinder through the inlet boundary condition. Additional details can be found in Nozawa & Tamura (2002) and Nozu & Tamura (2012). Figure 3(*a*) shows the mean velocity and turbulence intensity profiles at a location close to the inlet (i.e. $x/D = -7.4$) and figure 3(*b*) shows the power spectrum density compared with the Kármán spectrum. The turbulence intensity is defined as $I_u(z) = \sigma_u(z)/\bar{U}(z)$, where $\sigma_u(z)$ is the root mean square (r.m.s.) of the streamwise velocity and $\bar{U}(z)$ is the mean velocity at the height of z. The experimental and numerical results were generally consistent. Moreover, this consistency was maintained before approaching the cylinder.

To validate the method presented in this work, figure 4 compares the distributions of time-averaged and r.m.s. pressure coefficients (denoted $\bar{C}_p$ and σ_p, respectively) with the experimental results by Katsumura (as cited by Maruyama *et al.* 2013) under similar inflow conditions. The subplots show distributions at different cylinder heights. The measurement heights are indicated in figure 4(*a*), where the black lines on the surfaces of the cylinder denote the locations of measurement in the present study and the red lines denote the experimental locations. The letters '(b)' and '(c)' with numbers, which appear next to the cylinder in figure 4(*a*), correspond to the subplots in figure 4(*b*) and 4(*c*), respectively. The current results agreed well with Katsumura's measurements. A comparison of total forces, Strouhal number and mean flow fields with the available experiments was conducted by Cao *et al.* (2019). In general, the flow field showed good qualitative agreement between the numerical and experimental PIV results (Sumner *et al.* 2017; Unnikrishnan *et al.* 2017). Concerning the symmetry along the plane of $y = 0$ in figure 4, the general symmetry of mean values was obtained even though the symmetry of the r.m.s. values was broken at some points. Obtaining the so-called 'strictly' symmetric distributions of physical quantities is particularly difficult for a surface-mounted cylinder immersed in a thick turbulent boundary layer at a high *Re*. The asymmetry can be readily found in the previous experimental studies at a high *Re*, particularly for the r.m.s. values, as with the infinite-length cylinder of Lee (1975) and Noda & Nakayama (2003) and the

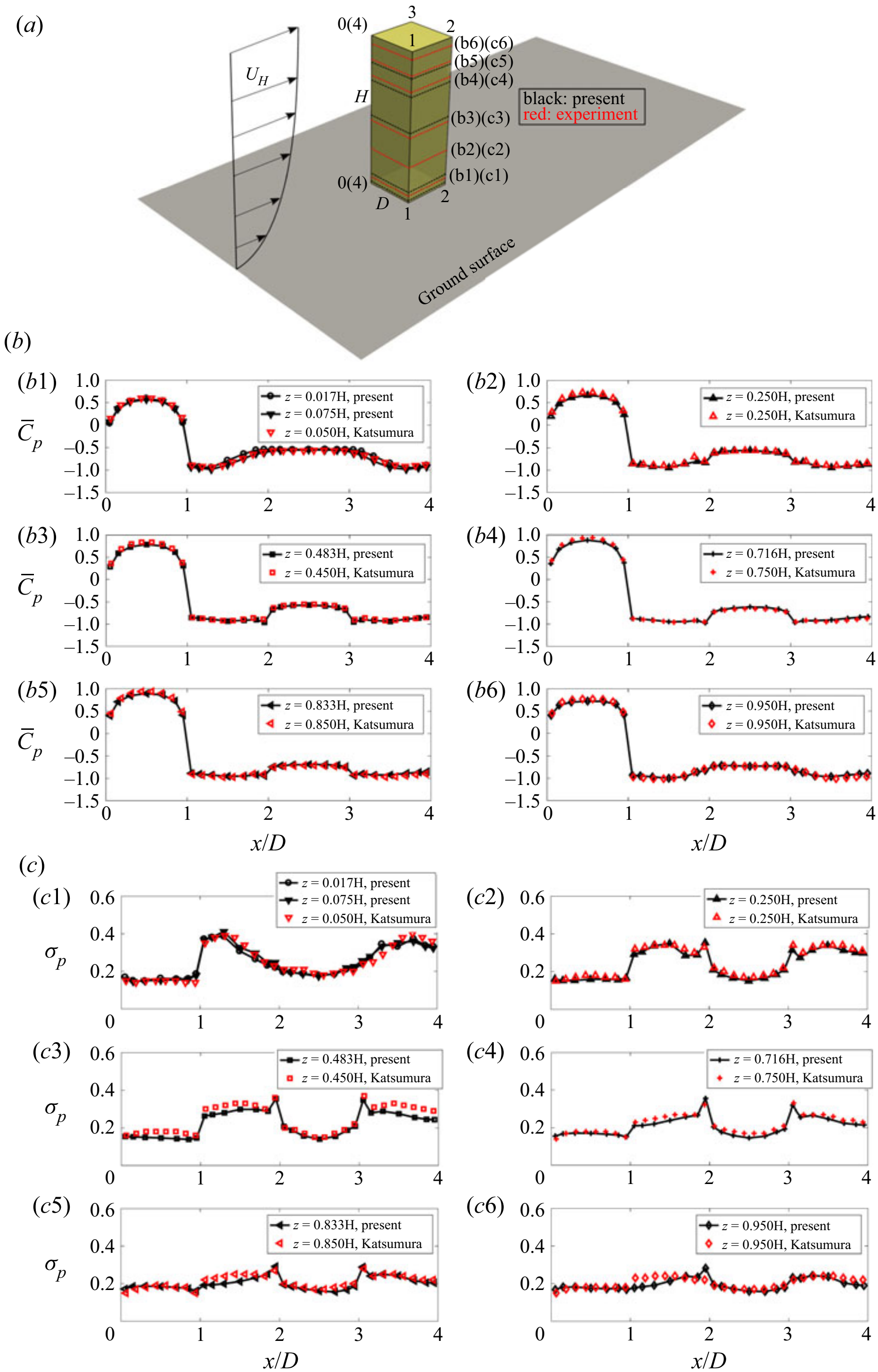

Figure 4. (*a*) Measurement heights in the present study (black lines) and the experiment (red lines). The letters '(b)' and '(c)' with numbers, which appear next to the cylinder, correspond to the subplots in panels (*b*) and (*c*), respectively. (*b*)–(*c*) Comparison of time-averaged and r.m.s. pressure distributions with the experiment, respectively, which are reproduced from Cao *et al.* (2019).

https://doi.org/10.1017/jfm.2021.1043 Published online by Cambridge University Press

finite-length cylinder of Wang *et al.* (2017). For the wake velocity, the r.m.s. values of streamwise and lateral components along the lateral direction were examined (not shown here for brevity), which showed very good symmetry in the wide region of the near wake.

3. Critical-point theory

In terms of the complexity of 3-D separated flows around a surface-mounted square cylinder, critical-point theory offers a rational means of describing the properties of a given vector field (e.g. velocity or skin-friction vector) obtained from the present high-resolution numerical simulation. The critical points are defined as the points in the flow field where the streamline slope is indeterminate and all components of the field are zero. Pioneering studies on critical points and applications to 3-D flow separation were performed by Oswatitsch (1958), Maskell (1955), Legendre (1956) and Legendre (1965). This approach has attracted increasing attention since 1956 (e.g. Lighthill 1963; Tobak & Peake 1982; Dallmann 1983; Dallmann & Schewe 1987; Perry & Chong 1987; Chong, Perry & Cantwell 1990; Délery 2001). A consistent description of the flow field is possible after the introduction of flow-topology notion, such as skin-friction lines, critical points, detachment (or reattachment) lines, separation (or reattachment) surfaces and topological rules. One motivation for the application of critical-point theory in this study is to obtain a rational description of complex 3-D separation flows around a surface-mounted bluff body in a time-averaged sense.

3.1. *Classification of critical points*

The term 'skin-friction line' is used in this study to represent the surface flow pattern, which is defined as the trajectory of the surface shear stress (or skin friction, which is the non-dimensional form of the shear stress). The classification of critical points in skin-friction lines is briefly reviewed following Délery (2001, 2013). Here, (x_1, x_2) denotes the orthogonal coordinates in a two-dimensional (2-D) space. In this study, the 2-D space is the surface of the cylinder or ground surface. For simplicity, the origin of (x_1, x_2) is located at the critical point under consideration and (τ_{w1}, τ_{w2}) denotes the vector of the surface shear stress in the space of (x_1, x_2). In the neighbourhood of the critical points, the first-order Taylor series expansion determines the behaviour of the vector field. The matrix of the velocity derivatives (i.e. Jacobian matrix) is shown in (3.1):

$$\boldsymbol{F} = \begin{bmatrix} \dfrac{\partial \tau_{w1}}{\partial x_1} & \dfrac{\partial \tau_{w1}}{\partial x_2} \\ \dfrac{\partial \tau_{w2}}{\partial x_1} & \dfrac{\partial \tau_{w2}}{\partial x_2} \end{bmatrix}. \tag{3.1}$$

Let λ_1 and λ_2 be the eigenvalues of $\boldsymbol{F}$, $\boldsymbol{I}$ the identity matrix and $\boldsymbol{e}$ the eigenvector,

$$(\boldsymbol{F} - \lambda \boldsymbol{I})\boldsymbol{e} = 0. \tag{3.2}$$

The eigenvalues can be determined by solving the characteristic equation $det(\boldsymbol{F} - \lambda \boldsymbol{I}) = 0$, which is expressed as

$$\lambda^2 + p\lambda + q = 0, \tag{3.3}$$

https://doi.org/10.1017/jfm.2021.1043 Published online by Cambridge University Press

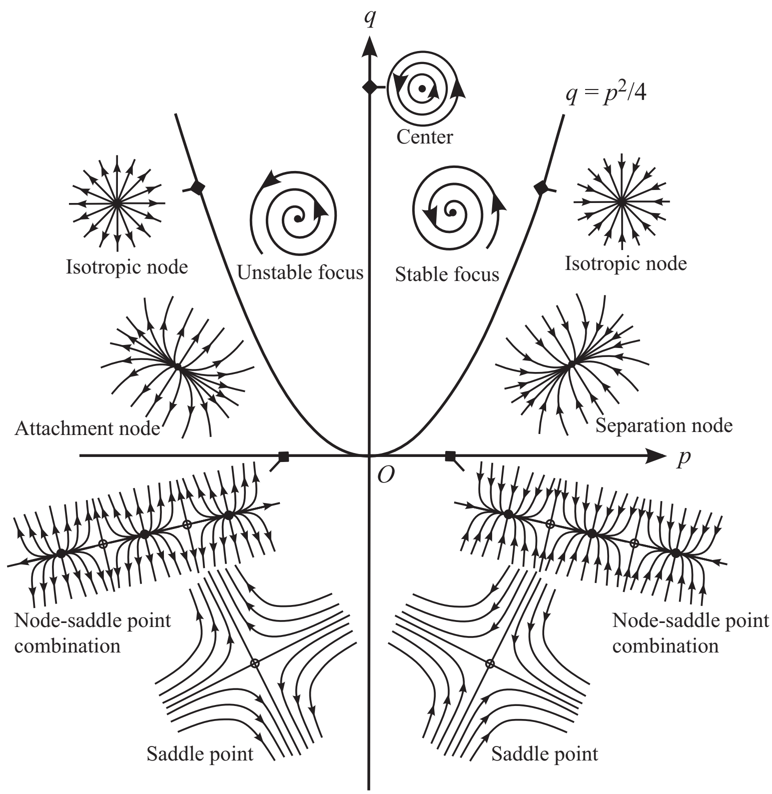

Figure 5. Critical-point classification in the chart of p–q, reproduced following Délery (2001).

where the discriminant is $p^2 - 4q$ and

$$p = -\left(\frac{\partial \tau_{w1}}{\partial x_1} + \frac{\partial \tau_{w2}}{\partial x_2}\right) = -tr(\boldsymbol{F}) = -(\lambda_1 + \lambda_2), \tag{3.4}$$

$$q = \left(\frac{\partial \tau_{w1}}{\partial x_1}\frac{\partial \tau_{w2}}{\partial x_2} - \frac{\partial \tau_{w1}}{\partial x_2}\frac{\partial \tau_{w2}}{\partial x_1}\right) = det(\boldsymbol{F}) = \lambda_1\lambda_2. \tag{3.5}$$

The characteristics of the skin-friction lines around the critical point are determined by the eigenvalues λ_1 and λ_2. The properties of λ_1 and λ_2 are represented in the chart of p–q. Figure 5 shows the classification of the critical points in a 2-D space, which is available in other publications (Perry & Chong 1987; Délery 2013). First, the node type is defined in the region below the parabola $q = p^2/4$ and above the axis $q = 0$. At the node point, all skin-friction lines have a common tangent that corresponds to one of the eigenvectors, excluding one line corresponding to the other eigenvector. A node is referred to as an attachment node when λ_1 and λ_2 are negative or as a separation node when λ_1 and λ_2 are positive. The special case is an isotropic node when $q = p^2/4$ (i.e. $\lambda_1 = \lambda_2$). Second, the saddle point type is defined in the region below the axis $q = 0$. All skin-friction lines avoid the critical point appearing in a hyperbolic shape, excluding the two lines passing through the saddle point. The skin-friction lines passing through the saddle are known as separation lines or separatrices. The occurrence of the saddle point is a major sign of flow detachment from the wall. According to Délery (2013), the flow is detached if the surface flow pattern contains at least one saddle point. Third, the focus type is defined in the region above the parabola $q = p^2/4$. The focus type is stable or unstable based on whether the skin-friction lines spiral into or out of the critical point, respectively. A special case is the centre, which is located on the axis $p = 0$. On the boundaries of the p–q chart (i.e. the parabola and axes), the critical points degenerate with structural instability; that is, an infinitesimal change in some parameters changes the type or direction of the critical point. In this study, the nomenclature of the critical points and separation/attachment lines generally follows that of Délery (2013). In other words, F, N, S, S', N', (A) and (S) represent foci, nodes, saddle points, half-saddle points, half-node points, attachment lines and separation lines, respectively.

3.2. *Basic rules of critical points*

The surface flow patterns should obey the basic rules (see details in Délery 2013). For example, the skin-friction lines must originate at one or several attachment nodes and terminate in either a focus or separation node. This excludes the separation lines of the saddle points. As a confirmation step, the formula determined by counting the number of critical points should be applied to a closed 3-D body, which is known as the 'Poincaré–Bendixson theorem' or 'hairy sphere theorem' and was introduced by Davey (1961) to address fluid-flow problems:

$$\sum N - \sum S = 2, \tag{3.6}$$

where $\sum N$ and $\sum S$ are the numbers of nodal points (nodes and foci) and saddles, respectively.

Note that (3.6) applies to a simply connected surface with a complexity equal to zero. The complexity of a surface is defined as zero if any closed curve traced on the surface can be reduced to a point by a continuous deformation without leaving the surface (Délery 2013). The complexity of the body is denoted by $\mathcal{P}$. If a body has a hole through it (such as a torus), the body has a complexity of one (i.e. $\mathcal{P} = 1$). If a body has two holes, then $\mathcal{P} = 2$. When the complexity $\mathcal{P}$ is considered, (3.6) is revised to (3.7) to be applicable to a body with or without holes passing through it:

$$\sum N - \sum S = 2 - 2\mathcal{P}. \tag{3.7}$$

For a 3-D body B placed on a plane P, several topological rules were recognised by Hunt *et al.* (1978). Surfaces B and P are treated as the upper surfaces of an imaginary 3-D body. There must be two nodes, one upstream and one downstream, at infinity on the imaginary lower surface of the imaginary 3-D body. For practical wind tunnels or numerical investigations of 3-D obstacles (as in the present study), the surface flow patterns on both the body and plane should satisfy the topological rule shown in (3.8). In this study, the surface-mounted square cylinder has no holes; thus, the total number of nodes should be the same as that of saddles on the combined surface of the square cylinder and the ground surface, that is, $(\sum N - \sum S)_{(P+B)} = 0$.

$$\left(\sum N - \sum S\right)_{(P+B)} = -2\mathcal{P}. \tag{3.8}$$

Equations (3.6)–(3.8) require the entire skin-friction field obtained from experiments or numerical simulations. Caution is required when applying (3.6)–(3.8) because most practical applications obtain only a part of the skin-friction field and rarely fulfil the aforementioned requirements. A useful practical rule was proposed by Hunt *et al.* (1978)

based on the 2-D plane sections of the flow, which are easily obtained in experiments or simulations. The half-nodes (N') and half-saddles (S') on the surfaces are introduced. The topological rule that obeys the kinematic principle for a 2-D section of the flow is expressed as

$$\left(\sum N + \frac{1}{2}\sum N'\right) - \left(\sum S + \frac{1}{2}\sum S'\right) = 1 - n, \tag{3.9}$$

where this 2-D slice of the flow is n-tuply connected. For a single-connected region, $n = 1$; for a doubly connected region, $n = 2$.

3.3. *Approximation of skin-friction lines*

In terms of surface flow patterns, the skin-friction lines are physical notions that should be adopted as much as possible. However, in practice, the limiting streamlines are sometimes used to approximate the skin-friction lines. In this study, a one-sided two-point finite difference is used to estimate the velocity derivative and skin friction. The feasibility and sufficiency are examined in Appendix C by comparing schemes with different accuracies. Hereafter, 'skin-friction lines' is the term used to describe the surface flow patterns. In addition, this study focuses on the time-averaged field and attempts to construct a mean separated flow organisation that satisfies the topological rules. One major reason for this is the similarity between some instantaneous vortex-shedding phases and the time-averaged field. This was illustrated in our previous study (see § 4.1 of Cao *et al.* 2019). When the shear layer is close to the side wall of the cylinder, the surface flow pattern on the side wall is similar to the time-averaged pattern. This means that the salient critical points in the time-averaged field can be found in their counterparts in the instantaneous fields. This motivates our study to emphasise the mean field before attempting to analyse complex transient flows. In addition, a large range of motion scales coexist in the transient flows at high *Re* values. The application of critical-point theory to complete instantaneous flow topology is very difficult (if not impossible).

4. Flow separation in front of the cylinder

The skin-friction lines on the ground surface are plotted in figure 6(*a*). Close-up views of the local regions (Zones A and B) are shown in figures 6(*b*) and 6(*c*). These features are described succinctly by an arrangement of nodes, foci and saddle points in figure 7.

The free-stream flow is first detached from the separation line (S_1) in figure 7(*a*), which originates from the saddle point S_1. The separation line (S_1) sustains the wrapped separation surface such that the primary horseshoe vortex is formed. The saddle point S_1 coincides with the node from which the streamlines emanate and comprise the horseshoe-vortex surface. The horseshoe vortex infinitely extends downstream along the separation line (S_1). The inner border of the primary horseshoe vortex is the attachment line (A_1) in figure 7(*a*). The upstream end of (A_1) is node N_1 on the ground surface flow pattern in figure 7(*a*) and the close-up in figure 7(*b*). A secondary horseshoe vortex arises between the attachment line (A_1) and the frontal wall of the cylinder. The secondary horseshoe vortex is oriented around the cylinder and travels downstream along the attachment line (A_1).

A close-up view of the ground-surface flow beside the side wall is shown in figure 7(*d*). Two nodes are observed within the recirculation zone: attachment node N_2 and separation node N_4. In particular, separation node N_4 has two non-orthogonal eigenvectors. Node N_4 is fed by attachment node N_2 and half-node N_1'. The free-stream flow is prevented from

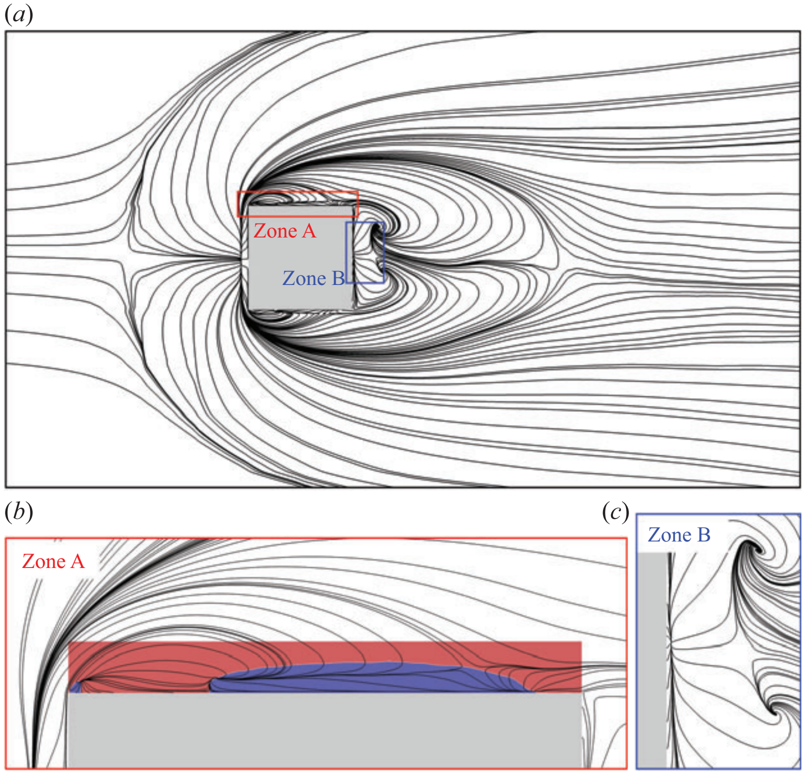

Figure 6. Skin-friction lines on the ground surface: (*a*) whole view; (*b*)–(*c*) close-up views of Zones A and B. In panel (*b*), blue indicates positive $\bar{U}$ and red indicates the reverse $\bar{U}$.

attaching to the trailing portion of the side wall by the saddle point S_2 and its separatrices (S_4) and (S_5). The skin-friction lines that detach from the trailing edge in figure 7(*d*) have two origins: one from the half-node N_1', the other from the outer free stream. The mechanism of S_2 formation is explained as follows. The shear layer in the higher position reattaches to the trailing portion of the side wall, partially evacuates downwards to the ground surface and propels the free stream immediately above the ground surface away such that it cannot attach directly to the side wall.

The detached flow from the trailing edge rolls towards the vortex foci F_1 and F_2 behind the cylinder. These two foci are segregated by the separation line (S_3) of the saddle point S_5. The combination of one saddle and two foci is commonly observed in the time-averaged wake of bluff bodies. The two foci are organised symmetrically. However, the real flows are never perfectly symmetric. In terms of the critical-point concept, the saddle-to-saddle connection (S_4–S_5) is structurally unstable (Perry & Chong 1987). The saddle-to-saddle connection can be easily removed by modifying the symmetry organisation and adding another separation line. However, this results in a topology that is too complex. Thus, symmetry is assumed in the wake (Délery 2013), which does not influence the description of other flow regions. The end of the separation line (S_3) is connected to node N_6 and the half-saddle S_{10}' in figure 7(*c*). This structure is associated with flow detachment from S_4 and flow attachment on N_6.

Finally, the locations of the main critical points shown in figure 7(*a*) are summarised in table 1. The flow separation point in front of the cylinder is located at $x/D = -1.73$, which

https://doi.org/10.1017/jfm.2021.1043 Published online by Cambridge University Press

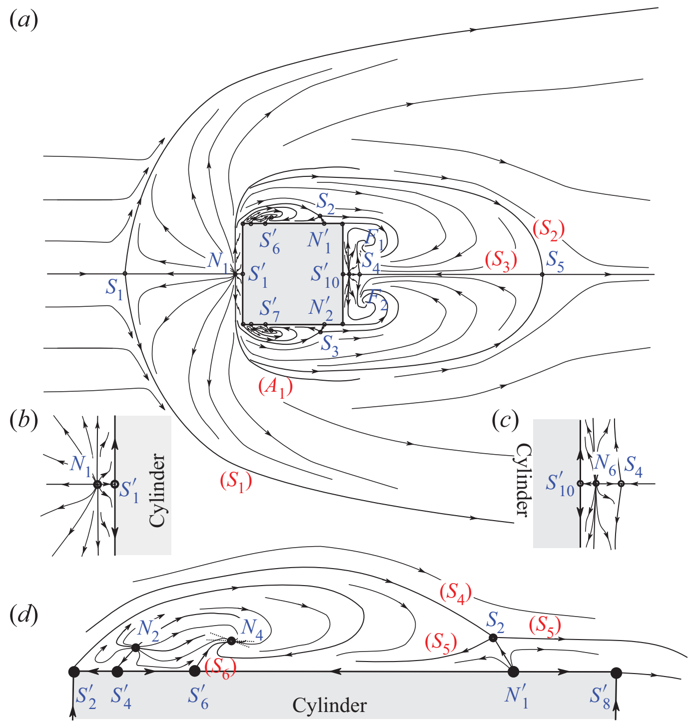

Figure 7. Surface flow pattern on the ground surface: (*a*) the whole view; (*b*) the close-up view of the central area immediately in front of the cylinder; (*c*) the close-up view of the central area immediately behind the cylinder and (*d*) the close-up view of the flow beside the side wall.

Critical points	$(x/D, y/D)$
Saddle in front of cylinder S_1	(−1.73, 0.05)
Node in front of cylinder N_1	(−0.57, −0.02)
Focus in the wake F_1	(0.76, 0.31)
Focus in the wake F_2	(0.80, −0.16)
Node immediately behind the cylinder N_6	(0.52, 0.04)
Saddle immediately behind the cylinder S_4	(0.71, 0.00)
Saddle in the wake S_5	(2.47, −0.08)

Table 1. Locations of the critical points in the surface flow pattern of the ground surface.

is more upstream than that in Ballio, Bettoni & Franzetti (1998). The main horseshoe vortex (centred at $x/D = -1.50$) is also more upstream than those of Ballio *et al.* (1998) and Sumner *et al.* (2017), possibly because of the much thicker turbulent boundary layer in this study. Furthermore, the numbering of the critical points in the surface flow pattern of the plane is five saddle points, two foci, six nodes, ten half-saddle points and two half-node points. The number of critical points is verified to satisfy the rule of (3.9), that is, $(\sum N + \frac{1}{2}\sum N') - (\sum S + \frac{1}{2}\sum S') = -1$, where $\sum N = 8$, $\sum N' = 2$, $\sum S = 5$ and $\sum S' = 10$.

5. Flow separation in the junction influence region

The 3-D effects of the wall pressure and surface flow pattern were investigated by Cao *et al.* (2019) based on the same flow configuration when $AR = 3$. The pressure distributions on the cylinder were classified into three categories from bottom to top: 'junction influence region' for $0 \lesssim z/D \lesssim 1.2$; '2D-like region' for $1.2 \lesssim z/D \lesssim 2.55$ and 'free-end influence region' for $2.55 \lesssim z/D \lesssim 3.0$. The border between two neighbouring regions corresponds to two notable saddle points in the surface flow pattern of the side wall. Following the classification of Cao *et al.* (2019), the 3-D flow separation is topologically described separately in terms of the junction influence region (in § 5) and free-end influence region (in § 6).

5.1. *Surface flow pattern*

The skin-friction lines on the walls of the cylinder are shown in figure 8. The arrow vector represents the direction of the in-plane velocity. The borders between the junction influence and 2-D-like regions and between the 2-D-like and free-end influence regions consist of two saddle points on the side wall, as indicated by S in figure 8(a). Furthermore, figure 8(c) zooms in to the local regions on the side wall (labelled as Zones D, E and F in figure 8a), where the arrows are plotted at every grid cell.

The aforementioned patterns of skin-friction lines on the walls of the cylinder are interpreted in figure 9 using the critical-point concept. At the centre of the frontal wall, as shown in figure 9(a), a pronounced attachment line (A_1) emanates from an attachment point ($z/D \approx 2.25$, out of the range of this figure). The attachment line (A_1) splits most of the skin-friction lines of the frontal wall into two separate portions along the positive and negative y directions. The attachment line (A_1) eventually connects with the saddle point S_1. The separation line (S_1) passing through the saddle point S_1 is the trace of the detachment of the downward flow induced by the stagnation effect of the ground surface. This detachment actually rolls to the secondary horseshoe vortex in front of the cylinder.

As a comparison, the surface flow pattern appears to be more complicated on the side wall, as shown in figure 9(b) and the close-up view in figure 9(d), where the flow is from left to right. First, the notable saddle point S_2 is located around the middle height of the cylinder (at $z/D \approx 1.2$) and is the border of the junction region with the 2-D-like region according to Cao *et al.* (2019). The separation lines (S_3) and (S_4) pass through the saddle point S_2. In particular, flow separation occurs from the separation line (S_4) as the skin-friction lines converge onto (S_4). The flow separation is confirmed again in terms of flow topology in the cross-section. The induced small-scale vortex is called the secondary separation vortex (SSV). The separation line (S_3) starts from node N_2 and continues roughly parallel to the attachment line (A_2) before turning towards the direction of the saddle point S_2. The positive streamwise velocity indicates the vortex upstream of the trailing edge between the attachment line (A_2) and trailing edge. Close to the leading edge, an attachment line (A_3) is observed, which emanates from node N_1. The separation line (S_4) winds towards focus F_1. Here, F_1 is a salient focus in the junction influence region because the skin-friction lines on the side wall of the cylinder that spiral into F_1 occupy a large portion of the junction influence region. This focus is the trace of the tornado-like vortex on the side of the cylinder (or 'inverted conical vortices' according to Okuda & Taniike 1993). The skin-friction lines in the region enclosed by the separation or attachment lines (S_3), (S_4) and (A_2) start from node N_2, bend in their direction and terminate at focus F_1. Near the ground surface, the saddle–focus–saddle–node connection S_3–F_1–S_4–N_2 is shown in figure 9(d). In this region, two sources of skin-friction lines exist. One source is the obvious attachment node N_2 and the other is the half-node point

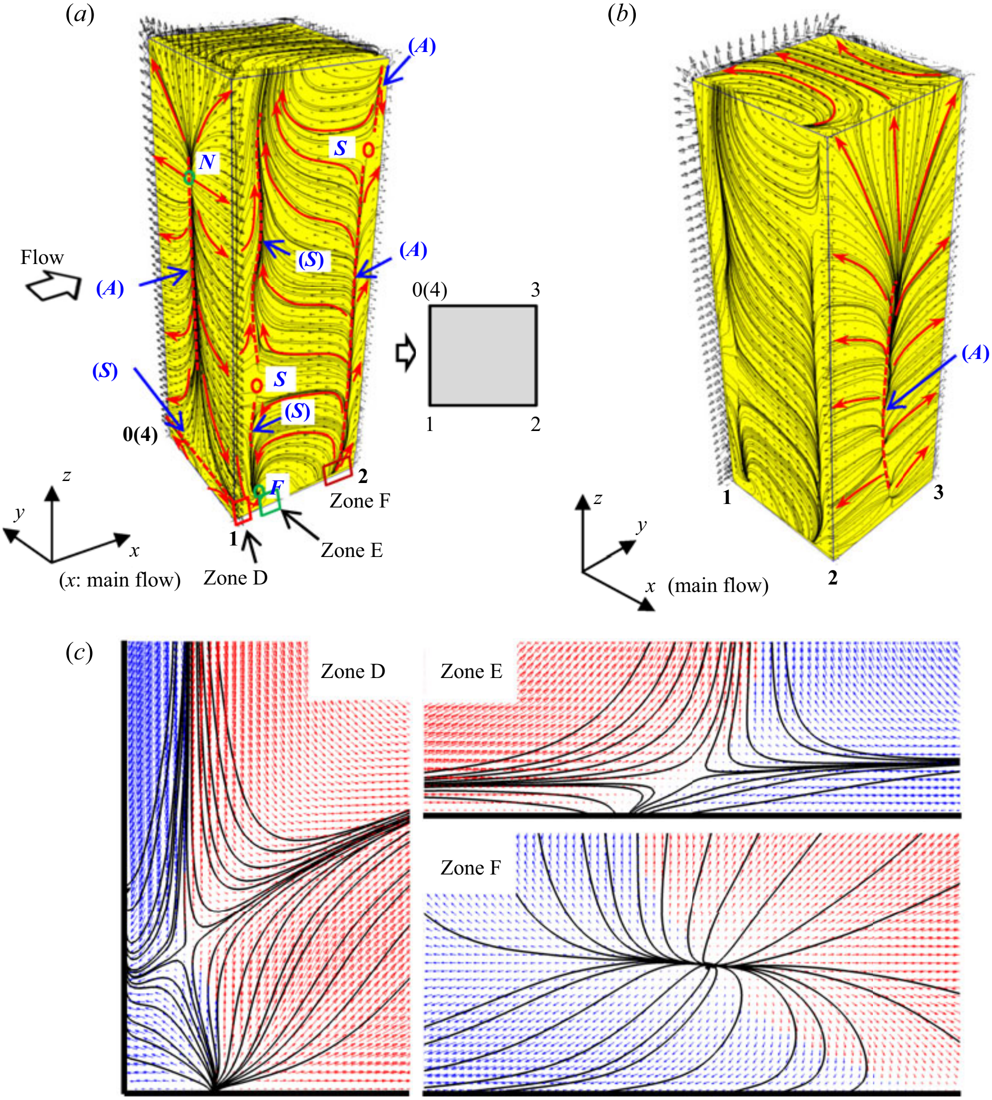

Figure 8. Skin-friction lines on the walls of the cylinder when $Re = 5 \times 10^4$. Panels (*a*) and (*b*) show two perspectives. Critical points are *S*, saddle points; *N*, nodal points; and *F*, foci. The dashed lines denote the (*S*) separation and (*A*) attachment lines. (*c*) Close-up view of the local regions on the side wall, including Zones D, E and F, where blue indicates positive $\bar{U}$ and red indicates reverse $\bar{U}$.

N_1' on the side wall. Moreover, this combination of S_3–F_1–S_4–N_2 ensures the side-wall surface flow is consistent with the surface flow pattern on the ground surface, as shown in figure 7(*d*). The half-saddle and half-node points identified on the side wall and ground surface are consistent in locations, that is, N_1', N_2' and S_1' on the side wall corresponding to S_4', S_6' and N_1' on the ground surface, as shown in figure 9(*d*).

The surface flow pattern on the back wall in the junction region is shown in figure 9(*c*). The attachment line (A_4) arising from the attachment node N_3 divides the attachment flows into two families moving towards two sides of the *y* coordinate. Below N_3, the sufficient height of the attachment region provides the condition for the formation of

https://doi.org/10.1017/jfm.2021.1043 Published online by Cambridge University Press

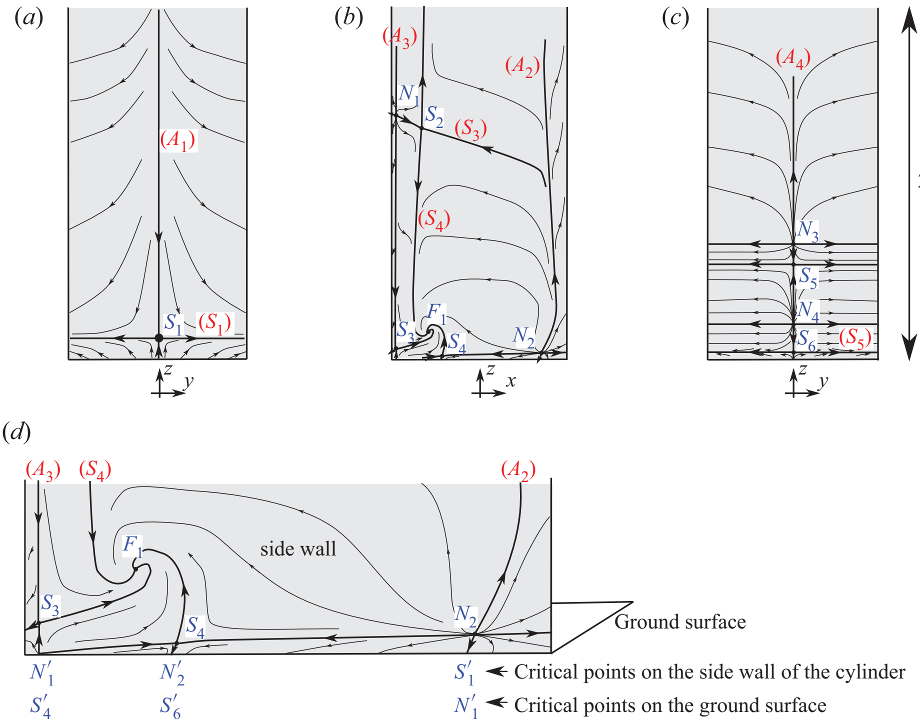

Figure 9. Surface flow pattern on the walls of the cylinder in the junction influence region: (*a*) frontal wall; (*b*) side wall, with flow from left to right; (*c*) back wall; (*d*) close-up view of the local region on the side wall.

3-D reattachment. The typical organisation of critical points is observed, that is, the saddle-node combination N_3–S_5–N_4–S_6 emphasised by Délery (2013), which belongs to the axis of $q = 0$ in the p–q chart. From the separation line (S_5) of the saddle point S_6 in the region located close to the ground surface, flow separation occurs and rolls up to generate a small-scale vortex immediately behind the cylinder. This small vortex corresponds to the focus F_3 in the symmetry plane when the vertical height is near the ground surface, as shown in figure 17.

5.2. *Three-dimensional separated flow topology*

For 3-D separation, the concept of a separation/attachment surface is adopted and denoted by (Σ) following the work of Délery (2013). The traces of separation/attachment surfaces on the body or ground surface are the separation/attachment lines. Similar to the surface flow patterns, we first visualise the numerical results. A 3-D separated flow topology is then constructed, which has topological consistency with the surface flow patterns and pseudo-streamlines in a cross-section.

The three-dimensionality in the junction region is so strong that the vortical structures and their relationships cannot be easily identified. Flow is visualised in a relatively neat manner in figure 10. Only half of the flow ($y \geq 0$) is shown, considering the symmetry in the mean field. Figure 10 shows several basic components: the pseudo-streamlines in the horizontal cross-section perpendicular to the cylinder axis (x–y plane); pseudo-streamlines on a vertical slice perpendicular to the x coordinate; surface flow patterns on the side wall; and 3-D streamlines twining around the vortex cores. The horizontal cross-sections are

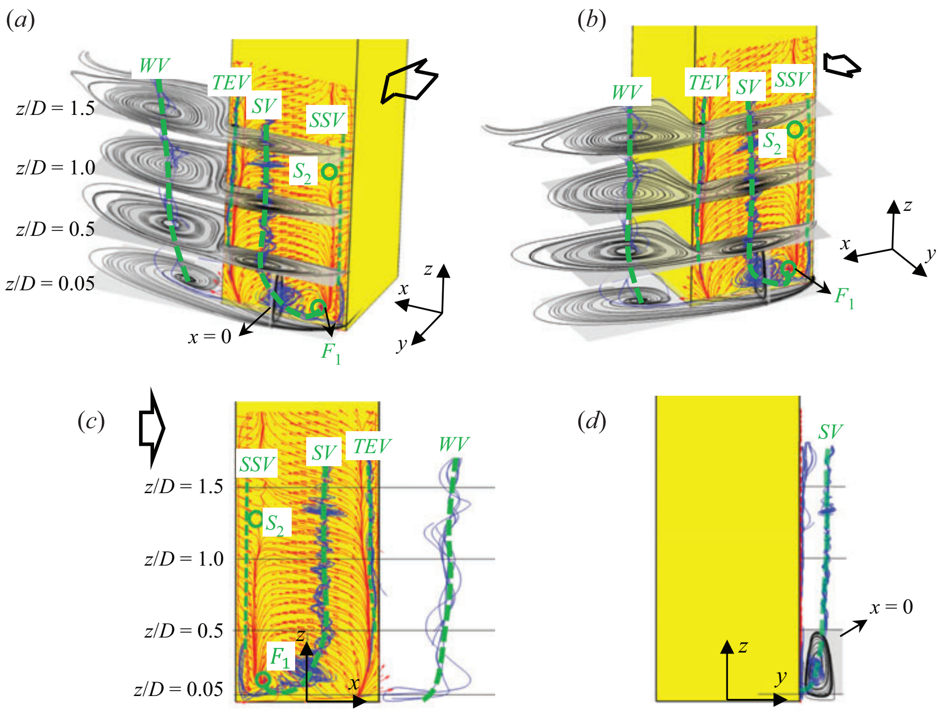

Figure 10. Flow visualisation of 3-D separation in the junction region. Panels (*a*)–(*d*) are from different perspectives. Here, S_2, saddle point on the side wall; F_1, focus on the side wall; *SV*, side vortex; *WV*, near-wake vortex; *TEV*, trailing-edge vortex; *SSV*, secondary separation vortex.

located at $z/D = 0.05, 0.5, 1.0$ and 1.5, and the vertical slice is located at $x = 0$. The vortex cores from the 3-D streamline swirl are identified using eigenmode analysis (Sujudi & Haimes 1995). Three primary vortices are emphasised and named: the side vortex, which originates from the focus on the side wall F_1 (*SV*); the trailing-edge vortex immediately upstream of the trailing edge of the cylinder (*TEV*); and the near-wake vortex behind the cylinder that emerges from the focus behind the cylinder (*WV*). The *SSV* is located just downstream of the leading edge and is relatively weak. The saddle point S_2 represents the border between the junction and 2-D-like regions.

The pseudo-streamlines in additional cross-sections are shown in the left-hand column of figure 11 to present the gradual evolution of the flow topology in the vertical direction. The flow topologies are constructed in the right-hand column of figure 11 using the critical-point theory to provide more rigorous insights. The number of critical points is shown. All flow topologies were checked and found to obey the topological rules (3.9) proposed by Hunt *et al.* (1978), where $n = 2$.

Figures 11(*a*) and 11(*b*) show the flow topologies in the cross-sections at $z/D = 0.16$ and 0.20. The insulation of the free stream from the side wall is observed in the ground-surface flow patterns, and is characterised by the existence of S_2 in figure 7(*d*). However, it is eliminated when the horizontal sectional plane is sufficiently removed vertically from the ground surface. As figure 11(*a*) shows, when $z/D = 0.16$, the free stream reattaches directly to the trailing portion of the side wall, and is characterised by flow reattachment on the half-saddle points S_7' and S_8' on the side walls. Moreover, the heights of $z/D = 0.16$ and 0.20 are above the secondary horseshoe vortex. The saddle point S_1 in figures 11(*a*)

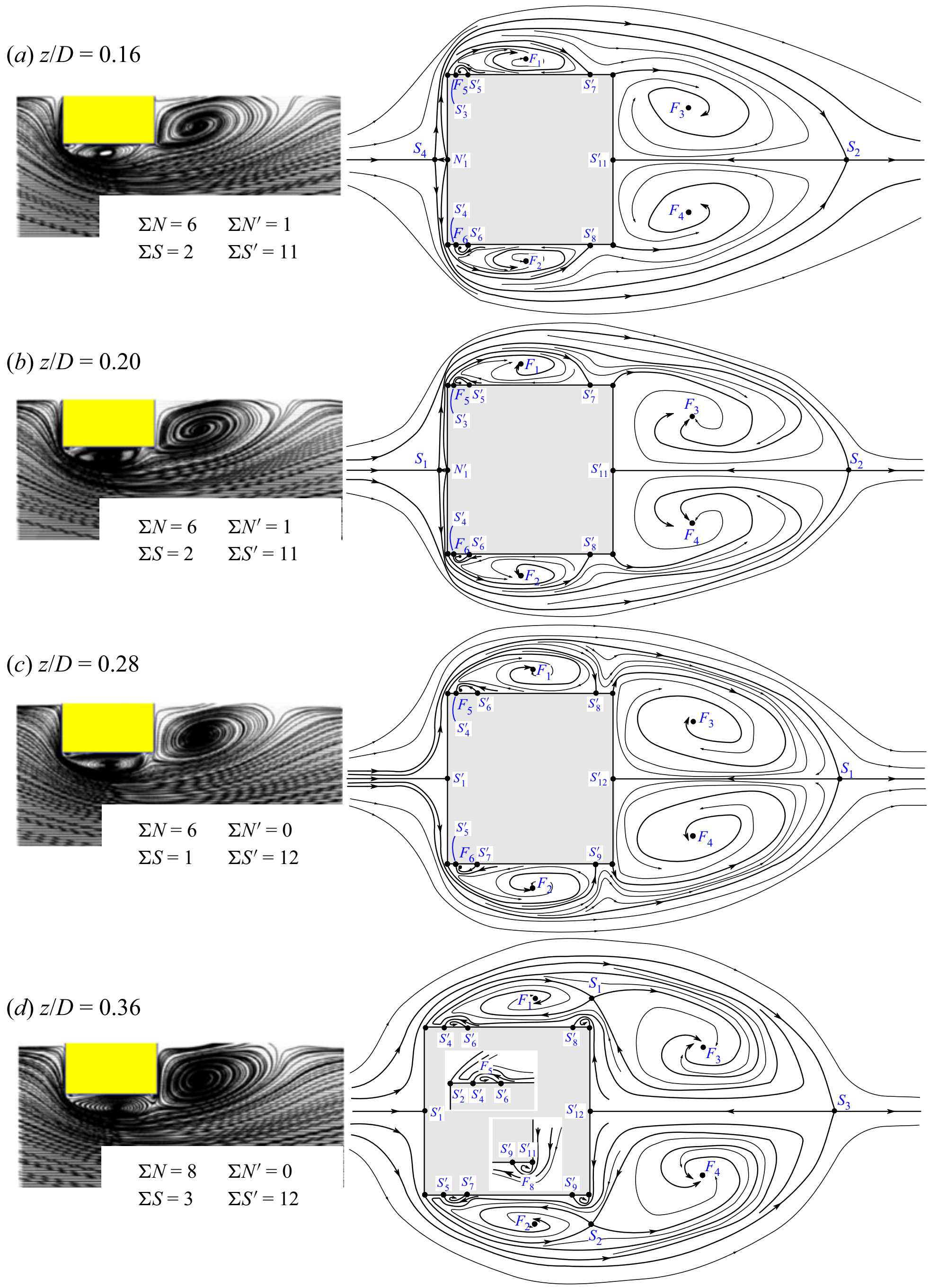

Figure 11. Flow topologies projected in the cross-sections at different heights above the secondary horseshoe vortex: (*a*) $z/D = 0.16$; (*b*) $z/D = 0.20$; (*c*) $z/D = 0.28$; (*d*) $z/D = 0.36$. The left-hand column shows the pseudo-streamlines from the numerical results; the right-hand column indicates the flow topology constructed using critical-point concepts, where the bold lines denote the separation lines. The number of critical points is also shown.

and 11(b) occurs in front of the cylinder, which is thought to be caused by the rapid increase in the thickness of the boundary layer attached to the frontal wall of the cylinder when approaching the separation line which maintains the secondary horseshoe vortex. The thick boundary layer flow is divided into two components: the inner component, which detaches from the leading edge of the cylinder and rolls up into the focus of the side vortex; and the outer component, which reattaches to the side wall upstream of the trailing edge and finally detaches again from the trailing edge. These two components are separated by separation lines ending at the half-saddle points S'_7 and S'_8 on the side walls. Figures 11(a) and 11(b) are topologically equivalent. However, the boundary layer thickness in figure 11(b) is obviously thinner, and the side and near-wake vortices are much wider. Because of the latter, the pseudo-streamlines near the flow reattachment region of the wall have greater curvature. When the height increases to $z/D = 0.28$ in figure 11(c), the reattachment region becomes shorter, the side and near-wake vortices are further widened, and the pseudo-streamlines near the reattachment region are curved more considerably and pushed outwards from the cylinder. Moreover, the saddle point in front of the cylinder is barely visible.

When $z/D = 0.36$ in figure 11(d), flow reattachment is no longer observed. Instead, a saddle point S_1 in figure 11(d) occurs between the side and near-wake vortices. The formation of the saddle point S_1 indicates the completeness of the changeover from the vertical flow region with to without reattachment. The separated flow from the leading edge of the cylinder is the primary source of the near-wake vortex. However, the separation line starting from the leading edge of the cylinder (i.e. starting from the half-saddle S'_2 in the subpanel of figure 11d) blocks the passage of the free stream into the side vortex foci F_1 and F_2. Instead, the main source of F_1 and F_2 is the reverse flow from the central wake. The reverse flow from the wake is easily detached from the trailing edge and forms trailing-edge vortices (see F_8 in the subpanel of figure 11d). The attachment points (attachment lines in 3-D space) of the trailing-edge vortices are indicated using half-saddle points S'_8 and S'_9 in figure 11(d). The reverse flow subsequently detaches from the half-saddle points S'_6 and S'_7, such that focus F_5 is generated in the subpanel of figure 11(d). Note that F_5 is the trace of the SSV.

The flow topology shown in figure 11(d) is applicable to the 2-D-like region of the surface-mounted and infinite-length square cylinders. Huang *et al.* (2010) proposed a topological flow pattern based on visualisations of both their surface oils and limited-resolution PIV (van Oudheusden *et al.* 2008). However, the study failed to consider the trailing-edge vortex. The newly proposed flow topology resembles the general flow pattern obtained by van Oudheusden *et al.* (2008) and Huang *et al.* (2010), and allows for small-scale vortices used in the previous high-resolution numerical simulations by Trias *et al.* (2015), Cao & Tamura (2016) and Cao, Tamura & Kawai (2020).

The flow topologies in the cross-sections of figure 11 are consistent with the surface flow patterns on the walls of the cylinder, as shown in figure 9. The corresponding relationship between the critical points in the flow topologies in the cross-sections and the separation/attachment lines on the walls of the cylinder is summarised as follows, where $\Leftrightarrow$ represents the corresponding relationship:

(1) N'_1 in figures 11(a) and 11(b) and S'_1 in figures 11(c) and 11(d) $\Leftrightarrow$ attachment line (A_1) on the frontal wall in figure 9(a);
(2) S'_3 and S'_4 in figures 11(a) and 11(b) and S'_4 and S'_5 in figures 11(c) and 11(d) $\Leftrightarrow$ attachment line (A_3) on the side wall in figure 9(b);
(3) S'_5 and S'_6 in figures 11(a) and 11(b) and S'_6 and S'_7 in figures 11(c) and 11(d) $\Leftrightarrow$ separation line (S_4) on the side wall in figure 9(b);

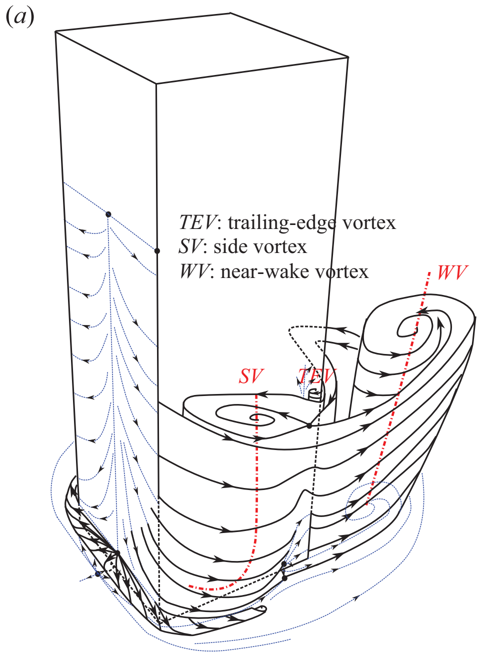

Figure 12. Three-dimensional separation surfaces in the junction region, including the near-wake, side, trailing-edge and secondary horseshoe vortices: (*a*) covered by the outer separation surface; (*b*) with the removal of the outer separation surfaces.

(4) S_7' and S_8' in figures 11(*a*) and 11(*b*) and S_8' and S_9' in figures 11(*c*) and 11(*d*) $\Leftrightarrow$ attachment line (A_2) on the side wall in figure 9(*b*);
(5) S_{11}' in figures 11(*a*) and 11(*b*) and S_{12}' in figures 11(*c*) and 11(*d*) $\Leftrightarrow$ attachment line (A_4) on the back wall in figure 9(*c*).

Based on the aforementioned observations, the 3-D separation surfaces that constitute the side and near-wake vortices are shown in figure 12, where panel (*a*) is covered by the outer separation surface and panel (*b*) focuses on the inner flow with the removal of the outer separation surface. In addition, the secondary horseshoe vortex proceeds out of the side vortex and then infinitely downstream. Because of the rotation effects of the side vortex and the curved but upward direction of the side vortex core, the separation node (N_4 in the ground-surface flow pattern in figure 7*d*) is formed by the attraction effect from the side vortex. Consistency is confirmed among the separation surfaces, the surface flow patterns on the ground plane and walls of the cylinder and the projected flow field in the cross-sections.

6. Flow separation in the free-end influence region

6.1. *Surface flow pattern*

The skin-friction lines on the walls of the cylinder in the free-end influence region are shown in figures 8(*a*) and 8(*b*) and are interpreted in figure 13. The border between the 2-D-like and free-end regions is indicated by saddle point S_7 in figure 13(*c*).

Node point N_5 in figure 13(*b*) is the stagnation point on the frontal wall, which is located at $z/D = 2.25$. All skin-friction lines spread out from N_5. Two attachment lines (A_1) and (A_2), which originate from N_5, correspond to two orthogonal eigenvectors of

https://doi.org/10.1017/jfm.2021.1043 Published online by Cambridge University Press

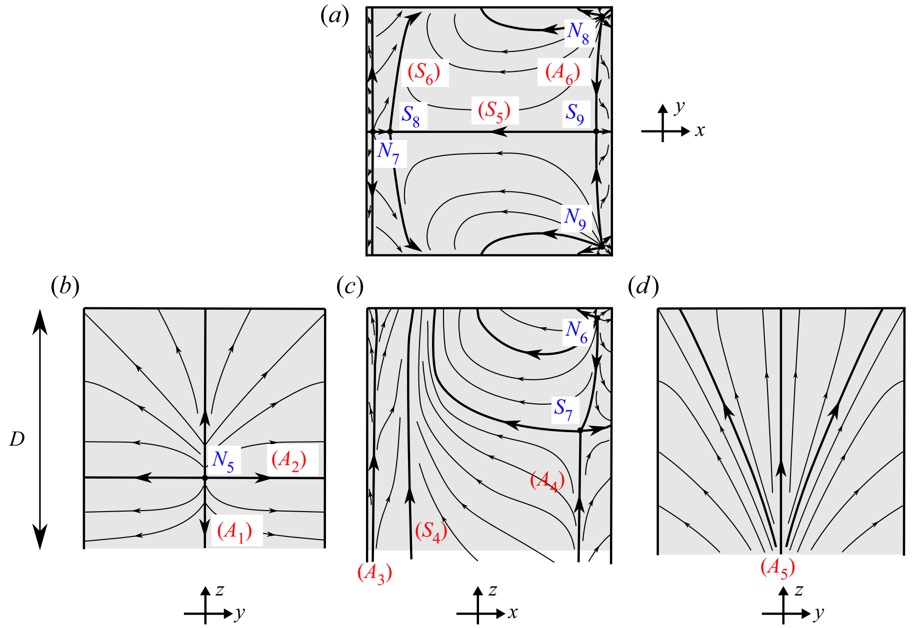

Figure 13. Surface flow pattern on the walls of the cylinder in the free-end influence region: (*a*) upper wall; (*b*) frontal wall; (*c*) side wall, with flow from left to right; (*d*) back wall.

the node point and divide the streamlines. The flow topology on the side wall is shown in figure 13(*c*). The existence of separation and attachment lines (A_3), (S_4) and (A_4) in the junction influence region implies two small-scale vortices next to the side wall of the cylinder (i.e. the *SSV* F_5 and the trailing-edge vortex F_8 in figure 11*d*). Above the saddle point S_7, a trailing-edge vortex is obtained from the flow separation and reattachment between the attachment line connecting S_7 and N_6 and the trailing edge of the cylinder. However, the fluid inside the trailing-edge vortex flows downwards. The size of the trailing-edge vortex in the free-end region becomes considerably smaller than that in the 2-D-like region. In the upstream portion of the side wall, most of the skin-friction lines emanate from node N_6 and change their direction from downwards to upwards. The skin-friction lines on the back wall in figure 13(*d*) are dominated by the near-wake vortex, and consequently flow upwards. The skin-friction lines are assumed to be symmetric around the attachment line (A_5) which emerges from node point N_3 in figure 9(*c*).

The surface flow patterns on the frontal, side and back walls are consistent with the top wall of the cylinder, as shown in figure 13(*a*). Towards the leading edge, the skin-friction lines curve outwards from the centreline of the prism. For simplicity, the flow topology is assumed to be symmetric around the separation line (S_5) connecting saddle points S_8 and S_9. However, the symmetry holds only theoretically because of the structural instability of the saddle-to-saddle connection S_8-to-S_9. The attachment line (A_6) implies the attachment of the reverse flow from the back wall which is driven by the near-wake vortex. The reverse flow enters the recirculation zone and separates again from the separation line (S_6). The process is the same as in the generation of vortex foci F_5 and F_8 in figure 11(*d*). Most of the skin-friction lines have the same tendency as the PIV measurements of a surface-mounted cube by Depardon *et al.* (2005) and of a surface-mounted square cylinder in a thin turbulent boundary layer by Sumner *et al.* (2017). The differences are observed only in regions close to the cylinder edges, where these regions are sensitive to the measurement technique and

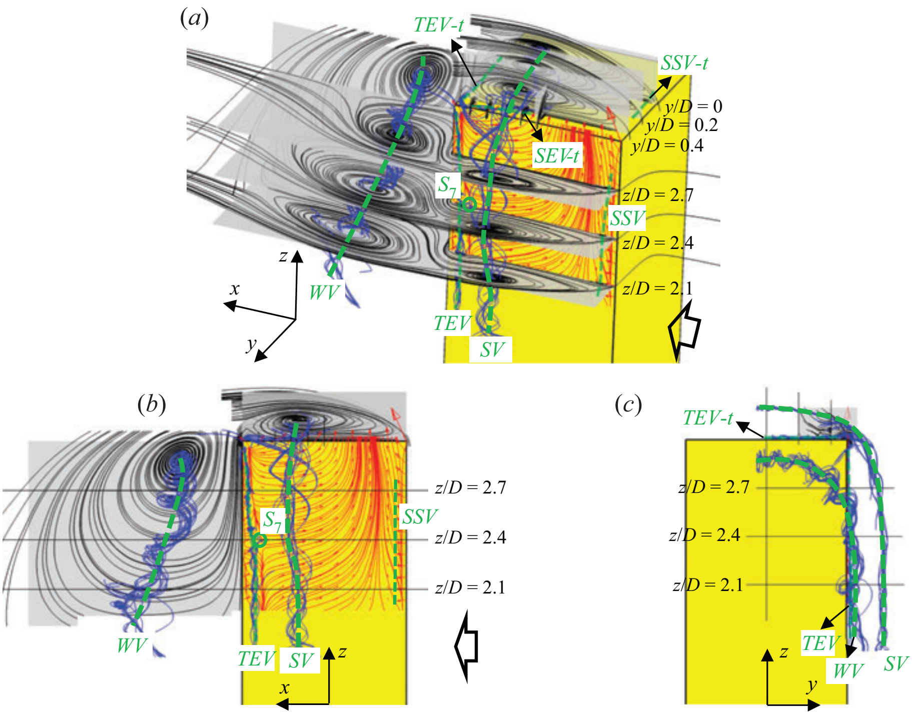

Figure 14. Flow visualisation of 3-D separation in the free-end region. Panels (*a*)–(*c*) are from different perspectives. Here, S_7, saddle point on the side wall; *SV*, side vortex; *WV*, near-wake vortex; *TEV*, trailing-edge vortex; *SSV*, secondary separation vortex. The vortex name followed by '-*t*' denotes the vortex above the top wall (i.e. *TEV*-*t*, side-edge vortex above the top wall; *SSV*-*t*, *SSV* above the top wall; *SEV*-*t*, side-edge vortex above the top wall.)

distance from the wall. In this study, the flow topology in figure 13(*a*) is constructed after a special close-up view of the local regions is examined near the edges of the cylinder when considering the topological consistency with the surface flows on the other walls of the cylinder. The same combination N_7–S_8–S_9 in the centreline of the top wall is consistent with Depardon *et al.* (2005) when $h = 0.008D$, but it was not observed by Sumner *et al.* (2017) when $h = 0.016D$.

6.2. *Three-dimensional separated flow topology*

Figure 14 presents a flow visualisation of the free-end influence region. The horizontal cross-sections are located at $z/D = 2.1$, 2.4 and 2.7, and the vertical slices are positioned at $y/D = 0$, 0.2 and 0.4. Saddle point S_7 represents the border between the 2-D-like and free-end influence regions. The cores of vortex structures wrapped by 3-D streamlines are emphasised and named in figure 14. Two vortices are produced by the main flow separation, namely, the side (*SV*) and near-wake (*WV*) vortices. Several small-scale vortices are produced by the secondary flow separation inside the recirculation region: the trailing-edge vortex next to the side wall (*TEV*), the vortex induced by the secondary separation next to the side wall (*SSV*), the trailing-edge vortex above the top wall (*TEV*-*t*), the side-edge vortex above the top wall (*SEV*-*t*) and the vortex induced by the secondary separation above the top wall (*SSV*-*t*). The side-edge vortex (*SEV*-*t*), which became weaker

https://doi.org/10.1017/jfm.2021.1043 Published online by Cambridge University Press

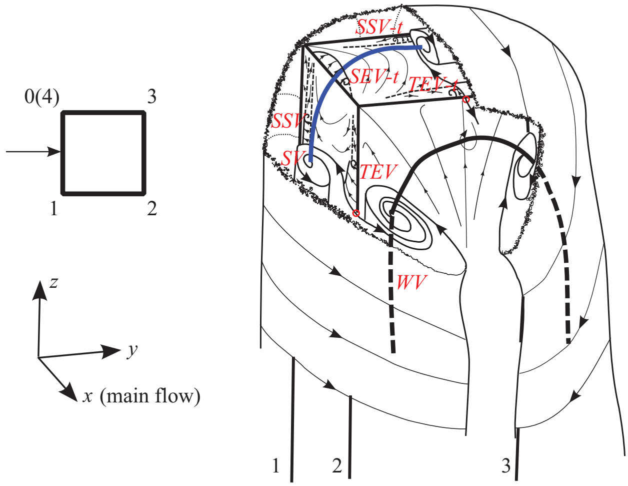

Figure 15. Three-dimensional separated flow topology in the free-end influence region. The abbreviations of vortices are referred to the caption of figure 14.

with a decreasing aspect ratio of the prism, was also reported by Sumner *et al.* (2017). Based on the flow visualisation, the 3-D separated flow topology is shown in figure 15.

The near-wake vortex (*WV*) behind the cylinder is first discussed. The near-wake vortex is composed of two vortex segments: one from the roll-up of the separated flow from the leading edge on the side wall and the other from the leading edge on the top wall. Interestingly, these two segments are connected. However, the vortex segment from the top wall is closer to the cylinder than that from the side wall. With the shape similarity, the near-wake vortex is also called an 'arch-type vortex' (Sakamoto & Arie 1983; Wang & Zhou 2009; Bourgeois *et al.* 2011; Rastan *et al.* 2017), with two standing legs corresponding to the roll-up from the sides of the cylinder and the head corresponding to that from the free end. The side vortex (*SV*) is maintained until it connects with the vortex inside the recirculation zone above the top wall. The *SV* originates from the focus F_1 on the lower upstream corner of the side wall. The sectional size of the side vortex is compressed when it is located near the side edge of the top wall. The compression propels the fluid near the side edge of the top wall towards the two sides, such that the skin-friction lines on the top wall curve towards the centreline and those on the side wall curve downwards.

Of the small-scale vortices, the trailing-edge vortex next to the side wall (*TEV*) warrants further discussion because its location is another signal of the classification between the 2-D-like and free-end influence regions, in addition to the aforementioned signal of saddle point S_7. From figure 14(*b*), the trailing-edge vortex shows an obvious downstream movement above saddle point S_7, and is induced by the push of the fluid near the side edge of the top wall.

The topological rule proposed by Hunt *et al.* (1978) is examined for symmetry-plane flow in this study. For completeness, the numbering of critical points is derived again for the symmetry-plane flow following Hunt *et al.* (1978). Figure 16(*a*) shows the symmetry-plane flow above the ground surface. Only one of the node, saddle, half-node and half-saddle points are illustrated for simplicity of explanation, which does not influence the following derivation. The ground surface is denoted as *OP*, and the upper line *XY* indicates the upper boundary of the symmetry-plane flow. First, the space above the ground surface *OP* is mapped into the region *OPXY*, as shown in the upper part

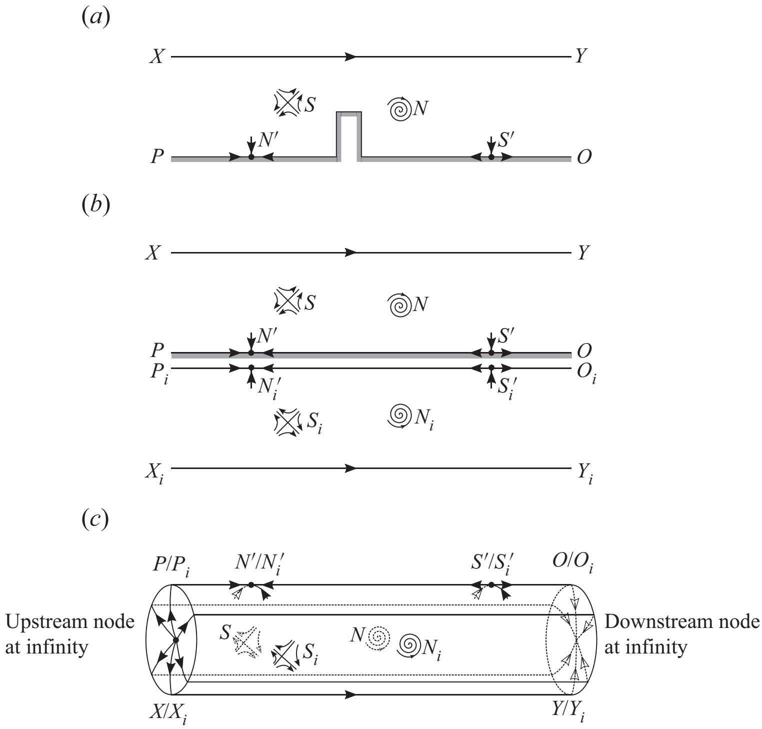

Figure 16. Schematic of mapping the flow above the surface to a closed body: (*a*) actual flow above the surface, where only one of the node, saddle, half-node and half-saddle points are illustrated; (*b*) flow region *OPXY* mapped from the actual flow by flattening *OP*, and the image system $O_iP_iX_iY_i$ formed by a mirror; (*c*) closed body with a complexity of zero created by wrapping the region *OPXY* and $O_iP_iX_iY_i$, where the imaginary upstream and downstream nodes at infinity are added to satisfy the topological principle.

of figure 16(*b*), by flattening the square cylinder. The nature of each singular point remains unchanged. Next, consider the image space $O_iP_iX_iY_i$ formed by a mirror and containing images of the nodes and saddles. The two spaces are then connected along *OP* and O_iP_i and wrap the surface into a cylinder until *XY* is connected with X_iY_i. The cylinder is shown in figure 16(*c*). The streamlines above the ground surface are regarded as the skin-friction lines covering the cylinder. Any skin-friction line must follow the principle in which it must terminate in either a focus or detachment node. Therefore, two imaginary nodes are created: upstream attachment and downstream detachment at infinity. The Poincaré—Bendixson theorem (i.e. where the number of nodes exceeds that of saddle points by two) is written in (6.1) for the skin-friction lines on the closed cylinder in figure 16(*c*) with a complexity of zero. Here, $\sum N$, $\sum N'$, $\sum S$ and $\sum S'$ are the numbers of critical points in the symmetry flow above the surface, as shown in figure 16(*a*). Additionally, $\sum N_i$ and $\sum S_i$ denote the numbers of nodes and saddles in the image space $O_iP_iX_iY_i$. The upstream and downstream nodes at infinity are considered by adding the two nodes to the first term on the left-hand side of (6.1). The relationships of $\sum N = \sum N_i$ and $\sum S = \sum S_i$ hold. Thus, (6.1) is rewritten as (6.2), which is used to check the number of critical points in the symmetry plane:

$$\left(2+\sum N+\sum N_i+\sum N'\right)-\left(\sum S+\sum S_i+\sum S'\right)=2, \tag{6.1}$$

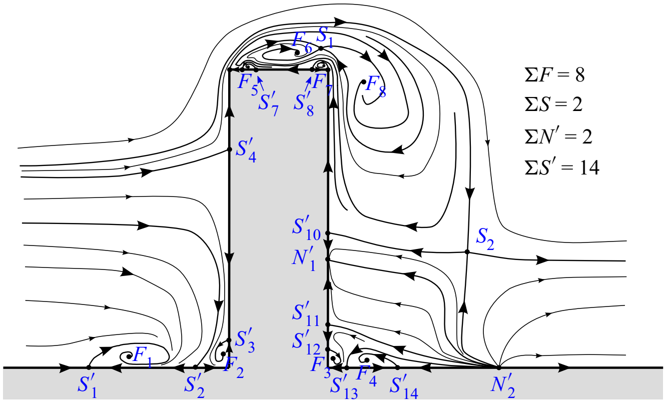

Figure 17. Flow topology in the symmetry plane when $Re = 5 \times 10^4$. The number of critical points is also shown.

$$\left(\sum N + \frac{1}{2}\sum N'\right) - \left(\sum S + \frac{1}{2}\sum S'\right) = 0. \tag{6.2}$$

Figure 17 shows the flow topology in the symmetry plane of the high-Re flow around surface-mounted square cylinder. The number of critical points is also shown in the figure and satisfies the topological rule, as shown in (6.2), that is, $(\sum N + \frac{1}{2}\sum N') - (\sum S + \frac{1}{2}\sum S') = 0$, where $\sum N = 8$, $\sum N' = 2$, $\sum S = 2$ and $\sum S' = 14$. The flow topology is consistent with the surface flow patterns on the ground plane, the walls of the cylinder and the 3-D separated flows. Half-saddle point S'_2 coincides with node N_1 on the ground-surface flow pattern in figure 7. The half-saddle points S'_{13} and S'_{14} on the ground surface, as viewed in the symmetry plane, coincide with the flow separation from S_4 and attachment on N_6 in figure 7(c). The half-node N'_2 behind the cylinder corresponds to the saddle point S_5 in the surface flow pattern of the ground plane in figure 7(a). In particular, for correspondence with vortices, the foci F_6 and F_8 correspond to the segment of the side vortex above the top wall and near-wake vortex (WV), respectively. The foci F_5 and F_7 correspond to the small-scale vortices SSV-t and SEV-t, respectively.

7. Discussion

7.1. *Tip vortices in the far and moderate wakes*

Few in-depth analyses of flow fields have been conducted when a surface-mounted square cylinder is immersed in a very thick boundary layer and at a high Re. In addition, a lack of agreement remains regarding the origin of streamwise tip and base vortices (if they exist) and their connection with the near-wake vortex structures (da Silva *et al.* 2020; Rastan *et al.* 2021). We investigated the properties of large-scale streamwise vortices behind the cylinder. Figure 18 shows the isosurface of the second invariant of the velocity gradient tensor $QD^2/U_\infty^2 = 0.01$, which is coloured by the streamwise vorticity ω_x. Considering the focus on large-scale vortices, the original time-averaged velocity field is filtered by a Gaussian filter with a width of $0.5D$ to remove the noisy small-scale vortices and obtain a clear visualisation of the Q criterion. It should be noted that filter widths of $0.25D$ and $0.1D$ are also tested and have no influence on the visualisation of large-scale vortices (including the near-wake vortex, tip and base vortices). Figure 18 clearly illustrates that only the tip vortices are present in the far and moderate wakes, whereas the base vortices

https://doi.org/10.1017/jfm.2021.1043 Published online by Cambridge University Press

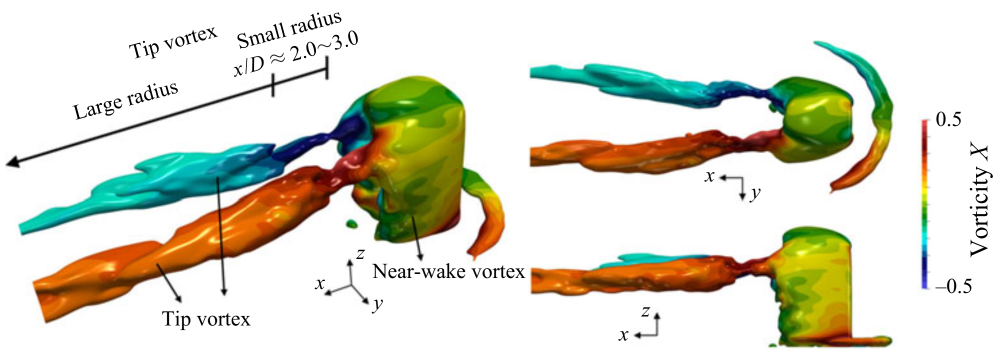

Figure 18. Isosurface of the second invariant of the velocity gradient tensor $QD^2/U_\infty^2 = 0.01$, which is coloured by the streamwise vorticity. Note that the velocity field is filtered by a Gaussian filter with a width of $0.5D$ to clarify the large-scale vortices.

are absent. The tip vortices are a pair of streamwise vortices with opposite rotational directions (identified by the opposite streamwise vorticity). Moreover, in comparison with the large radii in the far wake ($x/D > 3.0$), the tip vortices have smaller radii in the moderate wake ($x/D \approx 2.0$–3.0) just downstream of the recirculation zone behind the cylinder. Note that the horseshoe vortex is maintained up to $x/D > 8$, although it ends at $x/D \approx 0$ in figure 18 because it is weaker in strength than tip vortices and cannot be visualised by the sole isosurface. Details on the horseshoe vortex can be found in Baker (1979), Baker (1980), Ballio *et al.* (1998) and Escauriaza & Sotiropoulos (2011).

To identify the origin of the tip vortex, a visualisation method combining velocity streamlines and vortex lines is commonly used in the vorticity source analyses (Markowski *et al.* 2008; Tao & Tamura 2020). As previously mentioned, the tip vortex has two distinct regions of different radii: a region with a small radius when $x/D = [2.0, 3.0]$ and a region with a larger radius when $x/D > 3.0$. Thus, two source points for drawing velocity streamlines are selected at the centre of the tip vortex in two regions: $(x/D, y/D, z/D) = (2.5, 0.71, 2.42)$ and $(6.0, 1.2, 2.13)$. These are indicated by the black and red spheres in figure 19. Note that half of the flow field ($y > 0$) is shown for clarity. The streamlines through the two source points are represented by black and red lines. The vortex lines (whose tangents are everywhere parallel to the local vorticity vector) are shown in blue and pink, and their point sources are along the black and red streamlines with a constant streamwise interval of $1D$. In terms of the mean field, the variation in vortex lines along the velocity streamlines could provide information regarding the vorticity source and the evolution of vorticity from the ambient environment to the tip vortex.

The curved vortex lines originate from the separated flow region above the top wall of the cylinder and next to the side walls of the cylinder under the dominant shear effects, as shown by the lateral vorticity (ω_y) in figure 19(*b*). Notably, the vortex lines are in the outer partition of the shear-dominant region. They have positive ω_y above the cylinder and negative ω_z next to the cylinder. With increasing x, the central part of the vortex lines (i.e. the region of $y \approx 0$) is pressed down more considerably (see figure 19*c*) and travels slower than the outer and lateral parts of the vortex lines. The difference in downwash strength and convective velocity between the central and lateral parts causes distortion of the vortex lines and downstream stretching, as shown in figure 19(*a*). The positive ω_y and negative ω_z gradually change to positive ω_x, which corresponds to the rotation of the tip vortex. Notably, the aforementioned explanation could be applicable to the entire length of the tip

https://doi.org/10.1017/jfm.2021.1043 Published online by Cambridge University Press

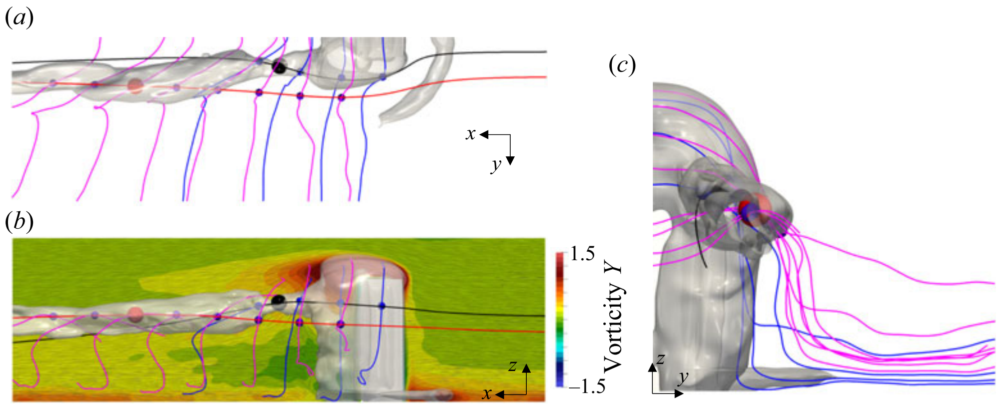

Figure 19. Vorticity source of the tip vortex, where only half of the domain ($y \geq 0$) is shown for clarity. The white 3-D isosurface is $QD^2/U_\infty^2 = 0.01$. The black and red lines are the velocity streamlines, whose source points are located at the centres of two regions of the tip vortex with small and large radii (i.e. $(x/D, y/D, z/D) = (2.5, 0.71, 2.42)$ and $(6.0, 1.2, 2.13)$, indicated by the black and red spheres, respectively). The blue and pink lines are the vortex lines, whose source points are located along the velocity streamlines at a streamwise interval of $1D$. (*a*) Top view; (*b*) side view, where the symmetry plane ($y/D = 0$) is visualised by the line integral convolution technique and coloured by the lateral vorticity component ω_y; (*c*) back view.

vortex with small and large radii, as the blue and pink vortex lines in figure 19 show a similar development mechanism in the streamwise vorticity.

In the present flow conditions (i.e. $Re = 5 \times 10^4$, the short cylinder with $H/D = 3$ and the very thick boundary layer with $\delta/D = 20.1$), the upwash is present in both the near ($x/D = 0.5$–2.0) and moderate ($x/D = 2.0$–3.0) wakes, as shown in figure 17. In contrast, base vortices are absent in the far wake. Thus, the wake structure belongs to the dipole model. This phenomenon is consistent with well-documented experimental and numerical studies when the aspect ratio is similar (Wang & Zhou 2009; Bourgeois *et al.* 2011; Kawai *et al.* 2012; Saeedi *et al.* 2014; Sumner *et al.* 2017), and Re is of the order of magnitude of 10^4. Figure 20 quantifies the amount of upward flow in the symmetry plane when $z/D \leq 1.0$, which is represented by the area-averaged vertical velocity in the sub-regions of the near, moderate and far wakes. The area-averaged vertical velocity is defined as $\iint_A \bar{W}/U_\infty \,\mathrm{d}x\,\mathrm{d}z/A$, where A is the area of each sub-region when the downward velocity is removed. The area-averaged vertical velocities in the near and moderate wakes are 0.0273 and 0.0133, respectively. However, the velocity rapidly decreases to a very low value of 0.0044 in the far wake, which is the main reason for the absence of base vortices.

7.2. *Relationship between tip and near-wake vortices*

The Q isosurface of the tip vortex in figure 18 appears to be directly associated with the near-wake vortex in the recirculation zone just behind the cylinder. However, some ambiguities exist in the relationship between the tip and near-wake vortices. For these reasons, figure 21 depicts the vorticity sources of the tip and near-wake vortices. The visualisation method of the tip vortex is the same as that shown in figure 19(*b*). The near-wake vortex is visualised in a similar manner as the tip vortex. The red line is the velocity streamline through the centre of the near-wake vortex in the horizontal plane (i.e. $(x/D, y/D, z/D) = (1.2, 0.53, 2.0)$) and the green lines are the vortex lines whose source points are along the red streamlines. According to figure 21, the vorticity of the near-wake vortex originates from the separated flow dominated by the shear effect, which surrounds

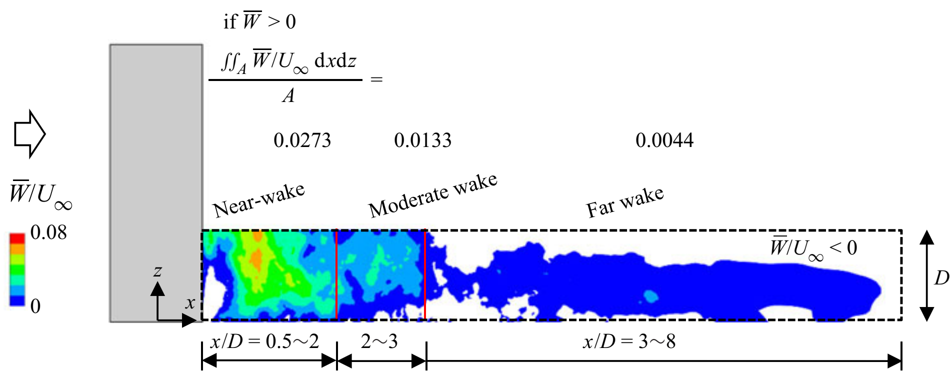

Figure 20. Quantification of the amount of upwash in the symmetry plane when $z/D \leq 1.0$. The colour indicates the distribution of vertical velocity in the region when $\overline{W} > 0$; the region of $\overline{W} < 0$ is not considered for the integration.

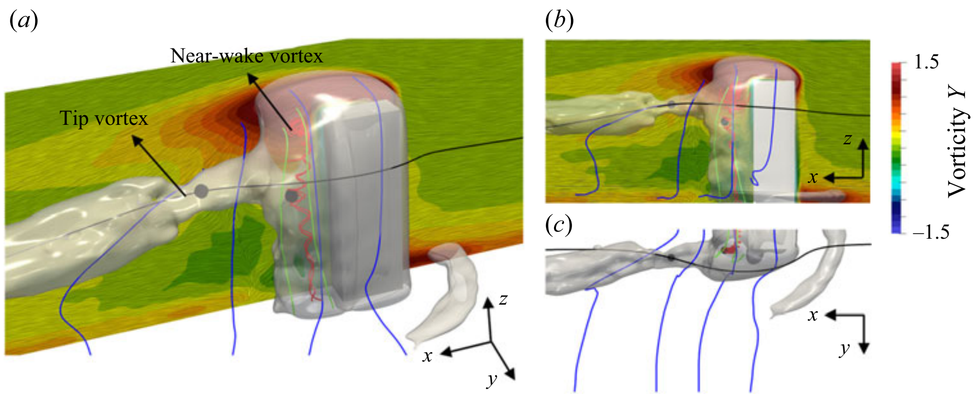

Figure 21. Relationship between the tip and near-wake vortices. The tip vortex is visualised in the same manner as in figure 19(*b*). The red line is approximately around the centre of the near-wake vortex. This is the streamline of velocity through the centre of the near-wake vortex in the horizontal plane, specifically at $(x/D, y/D, z/D) = (1.2, 0.53, 2.0)$, as indicated by the black sphere. The green lines are the vorticity lines along the red velocity streamline, which are plotted to illustrate the vorticity source of the near-wake vortex. (*a*) 3-D perspective, (*b*) side view and (*c*) top view.

the side and top of the cylinder. Basically, the vorticity source of the near-wake vortex is the same as that of the tip vortex, both being from the separated shear-layer region. However, figure 21 indicates that the vorticity of the tip vortex originates from the outer region of the shear-dominated separated flow, whereas the near-wake vortex originates from the inner region. In other words, the shear-layer flow with strong vorticity is separated into the near-wake and tip vortices.

The distribution of the near-wake vortex core is shown in figure 22, which is obtained by eigenmode analysis (Sujudi & Haimes 1995). It bends or inclines towards the cylinder at the top and bottom. Accordingly, it resembles the vortex-shedding model proposed by Wang & Zhou (2009). The bending at the bottom is restricted to the region of $z/D < 0.3$. Above this height, the vortex core is aligned with the axis of the cylinder until $z/D = 2.0$. When $z/D = 2$, the vortex has the largest size in the streamwise and lateral directions in figures 22(*b*) and 22(*c*). The inclined near-wake vortex when $x/D < 1.2$ and $z/D > 2.0$ indicates the existence of streamwise vorticity in the y–z plane. This is evidenced by the

https://doi.org/10.1017/jfm.2021.1043 Published online by Cambridge University Press

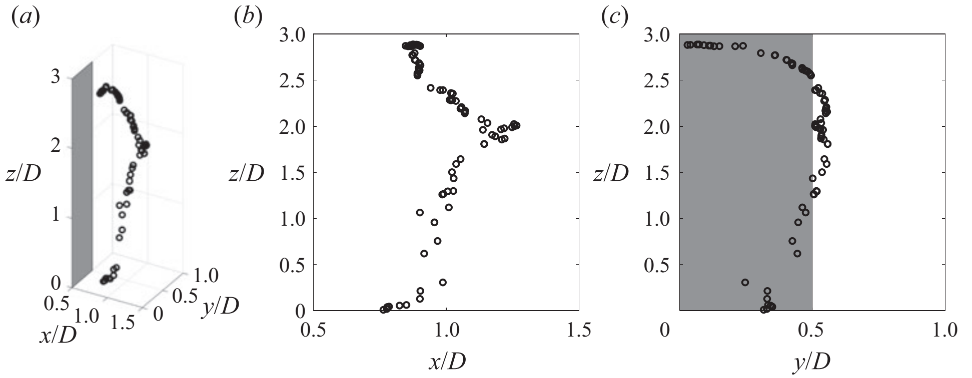

Figure 22. Distribution of the near-wake vortex core from the 3-D and projected views in the x–z and y–z planes.

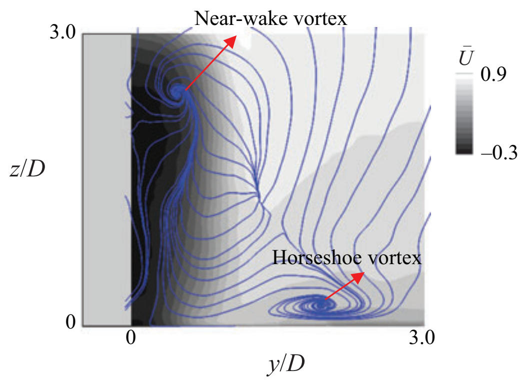

Figure 23. Flow in the y–z plane when $x/D = 1.0$, where the background greyscale refers to the streamwise velocity.

y–z plane when $x/D = 1.0$ in figure 23, where the focus is the projected near-wake vortex. Thus, it should be treated carefully when examining the streamwise vorticity in the near wake for the purpose of identifying the tip vortex, as it may not indicate the tip vortex but rather the projected component of the near-wake vortex. This type of situation is often encountered in experiments when data are limited and the tip vortex is identified by the streamwise vorticity projected in the vertical plane normal to the free-stream flow. The streamwise vorticity used to recognise the tip vortex may be true in the far wake because the near-wake vortex disappears and the tip vortex is primarily horizontal. However, the streamwise vorticity in the near wake is actually the projected near-wake vortex that inclines towards the cylinder.

7.3. *Reynolds number effects on upwash*

Relatively complete near-wall flow patterns were previously reported through high-accuracy simulations when the *Re* ranged from 40 to 1000 (Rastan *et al.* 2017; Zhang *et al.* 2017; Behera & Saha 2019; da Silva *et al.* 2020). This study is the first to provide a complete near-wall topological description at a high *Re* ($Re = 5 \times 10^4$). In this and the following sections, we discuss the variations in important flow features induced by the increase in *Re*. The *Re* featured by the start of unsteady flow of a finite-height square cylinder was previously reported to be higher than that of the infinite-length cylinder. Specifically, the critical *Re* of primary wake instability was previously suggested to be 75–200 for finite-height cylinders (Dousset & Pothérat 2010; Rastan *et al.* 2017; Zhang *et al.* 2017), whereas it was 46–50 for infinite-length cylinders (Bai & Alam 2018; Jiang & Cheng 2018; Jiang, Cheng & An 2018). Thus, the *Re* featured by the start of the laminar–turbulent transition of the after-body shear layer is expected to be higher than that of an infinite-length cylinder. Bai & Alam (2018) reported that the transition *Re* was 220 for the infinite-length square cylinder. Moreover, Zhang *et al.* (2017) and da Silva *et al.* (2020) performed systematic flow visualisations at $Re = 500$ and 1000. Therefore, this study focuses on *Re* values above 500.

An important aspect to consider is how the *Re* influences the upwash behind the cylinder. No upwash (identified by the existence of a wake saddle point in the symmetry plane) was observed in the low-*Re* simulations at $Re = 500$ and 1000 (Zhang *et al.* 2017; da Silva *et al.* 2020). Instead, the downwash directly touched the ground surface. However, in the present study, the upwash is clearly present when $Re = 5 \times 10^4$. The first impression of the upwash presence in this study may arise from the much thicker boundary layer ($\delta/D = 20.1$) than in the low-*Re* simulations ($\delta/D = 0.31$–0.43 when $Re = 500$ or 1000 in Zhang *et al.* 2017 and da Silva *et al.* 2020). This is mainly based on the finding that the upwash strength is proportional to the thickness of the boundary layer (Wang *et al.* 2006). Whether the *Re* affects the formation of the upwash may also be considered. To verify this possibility, we collected the previous and present results when $Re \geq 500$ in figure 24, including those of Wang *et al.* (2006), Wang & Zhou (2009), Bourgeois *et al.* (2011), Kawai *et al.* (2012), Hosseini *et al.* (2013), Uffinger, Ali & Becker (2013), Saeedi *et al.* (2014), Sumner *et al.* (2017), Zhang *et al.* (2017), Unnikrishnan *et al.* (2017), Zu & Lam (2018), Cao *et al.* (2019), da Silva *et al.* (2020), Yauwenas *et al.* (2019), Rastan *et al.* (2021), Behera & Saha (2021) and Zhao *et al.* (2021). The aforementioned data have a range of aspect ratios of $H/D = 2.7$–18.6. Note that figure 24 includes the data when the upwash (i.e. wake saddle point) exists, even though it is considered weak (e.g. Rastan *et al.* 2021). Surprisingly, the previously cited references show the clear existence of upwash in the near wake when $Re = O(10^4)$, even though the boundary layer thickness varies from very thin to very thick and includes the thicknesses of the low-*Re* simulations (Zhang *et al.* 2017; da Silva *et al.* 2020). Wang *et al.* (2006) measured the height of the saddle point S_2, as shown in figure 17, at $z = 1.2D$, $1.7D$ and $2.7D$. Bourgeois *et al.* (2011) observed the saddle point S_2 at $z = 1.4D$ and Sumner *et al.* (2017) reported S_2 at $z = 1.0D$. In the same order of *Re*, the present simulation gives a comparable height ($z = 1.1D$) of S_2 even though it has a much thicker boundary layer inflow. Thus, we argue that the thickness of the boundary layer is not the sole factor which determines the existence or strength of the upwash. Instead, an increase in the *Re* when $Re \geq 500$ more significantly affects the occurrence of upwash behind the cylinder and the boundary layer thickness quantitatively enhances the upwash strength. Nevertheless, additional parametric studies are required to assess the *Re* effects in the range of 500 to $O(10^4)$ when the aspect ratio and boundary layer conditions are the same. Rastan *et al.* (2017) and Zhang *et al.* (2017) investigated the effects of *Re* values but confined their studies to the low-*Re* region of $Re \leq 1000$. Their results showed that the upwash was gradually suppressed by the increase in *Re* when *Re* was above the critical *Re* between steady and unsteady flows. The conclusions regarding the effects of *Re* on upwash in the present study counter those of Rastan *et al.* (2017) and Zhang *et al.* (2017) because the present *Re* regime of $Re \geq 500$ is characterised by the occurrence of shear layer instability and is essentially different from those of Rastan *et al.* (2017) and Zhang *et al.* (2017).

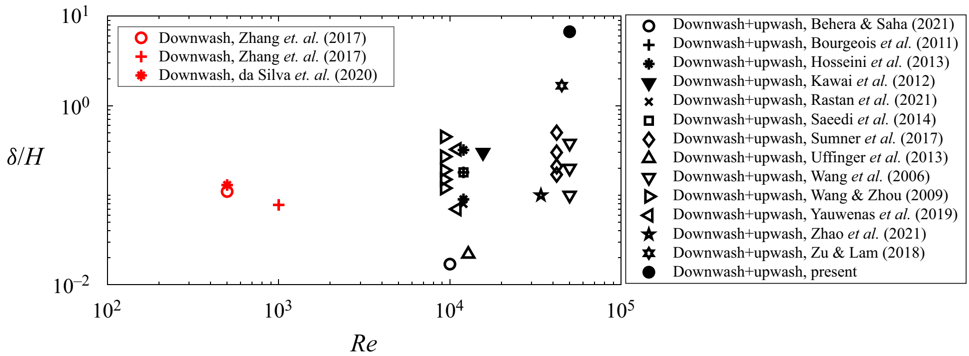

Figure 24. Compilation of upwash existence in the symmetry plane when $Re \geq 500$ and $H/D = 2.7$–18.6.

It is unclear why the upwash is present at high $Re = O(10^4)$ but absent at low $Re = 500$ and 1000. First, an explanation of the mechanism for upwash generation is attempted. At a high Re, the flow has a high potential to reattach to the trailing edge of the cylinder in the junction influence region, as clearly identified by the present numerical results (figure 11*a*). In comparison, the reattachment in the junction influence region was not reported by da Silva *et al.* (2020) when $Re = 500$. The smaller streamwise and lateral sizes of the near-wake vortex near the ground can also be observed in the distribution of the vortex core in figures 22(*b*) and 22(*c*). The shrinkage in the lower region leads to an axial flow along the near-wake vortex. The axial flow can then only proceed upwards to the middle height of the near wake because of the blockage of the ground surface. Eventually, the flow appears as a spiral escalation along the near-wake vortex, increasing its lateral size in the middle part, as shown in figure 22(*c*). The upwash observed in the symmetry plane is the projected flow of the upward spiral along the near-wake vortex. Second, the tendencies of the recirculation zone with increasing Re from 500 to $O(10^4)$ and their effects on the upwash generation at $Re = O(10^4)$ are discussed. The recirculation zone (or vortex formation length) decreases significantly with an increase in Re. The mean recirculation length at the middle height of the cylinder ($L_{f,mid}$) decreases from $6.13D$ to $4.81D$ when Re increases from 500 to 1000 (Zhang *et al.* 2017), where the mean recirculation length (L_f) is defined as the streamwise distance from the centre of the cylinder to the last point where the mean streamwise velocity is equal to zero. da Silva *et al.* (2020) reported $L_{f,mid} = 3.52D$, although a smaller value than that of Zhang *et al.* (2017) was claimed because of the different thicknesses of the approaching boundary layer. In comparison, in the present study, $L_{f,mid}$ decreases to $1.95D$ when $Re = 5 \times 10^4$, which is much smaller than those in previous studies at a low Re. It is expected that both vertical legs and the horizontal head of the near-wake vortex behind the finite-length square cylinder become smaller when the Re increases from 500 to $O(10^4)$. The interaction between the two vertical legs of the near-wake vortex increases with an increase in Re and compresses the gap between the two vertical legs. Therefore, in contrast with the low-Re cases, the horizontal head of the near-wake vortex with a reduced size cannot reach the ground surface at a high Re of $O(10^4)$. Eventually, both downwash and upwash can be observed in the near and moderate wakes at Re of the order of magnitude of 10^4.

7.4. *Reynolds number effects on near-wall flows*

In terms of the near-wall flow of finite-height cylinder, differences can be observed in the junction influence region between the low- and high-Re flows. In particular,

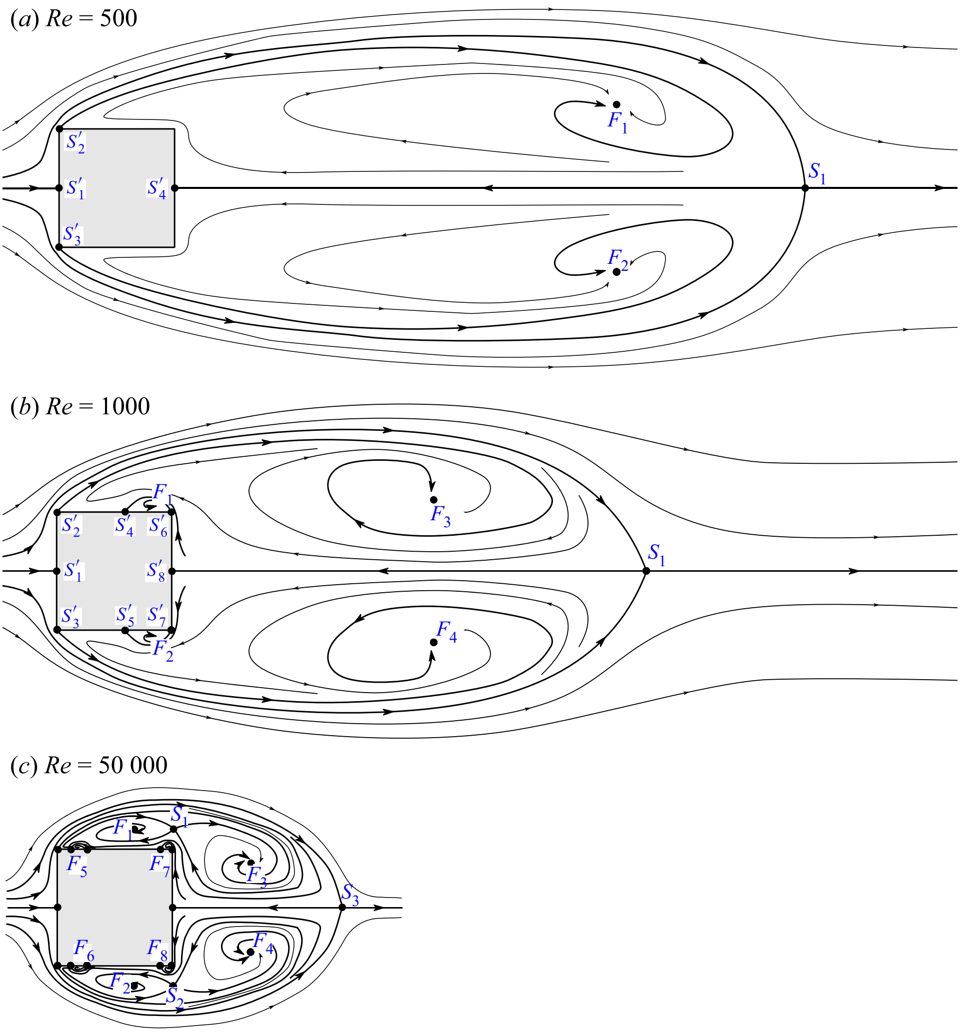

Figure 25. Flow topology on the cross-sections of the middle height of the cylinder: (*a*) $Re = 500$, inferred from the flow visualisation of Zhang *et al.* (2017); (*b*) $Re = 1000$, inferred from the flow visualisation of Zhang *et al.* (2017); (*c*) $Re = 50\,000$ in the present study.

in da Silva *et al.* (2020), no reattachment of flow was observed on the trailing part of the side wall in the junction influence region when $Re = 500$. However, reattachment is clear in the present study (see figure 11*a*), and the reattachment compresses and strengthens the side vortex (also called a tornado-like vortex). This results in notable foci on the side walls (see F_1 in figure 10), which are absent in the low-*Re* flows. Thus, the *Re* effects cannot be ignored when considering the inverted conical vortex, which is related to the negative peak pressure on the side walls. In addition, the reattachment of the flow induced by the increase in the *Re* is consistent with the shrinkage of the near wake.

Figure 25 shows the construction of flow topology on the cross-section of the middle height based on the low-*Re* flow visualisations by Zhang *et al.* (2017) and the present study. The flow topologies obey the rules of critical points. In comparison, the present high-*Re* flow possesses many small-scale vortices in addition to the shrinkage of the recirculation zone. The inertial force of fluid particles increases with an increase in the *Re* (and shrinkage of the recirculation zone), which tends to separate easily from the wall or edges of the body. The small-scale vortices include the leading- and trailing-edge vortices on the side walls. The trailing-edge vortex formation squeezes out the reverse flow from the wake, gradually cutting off the connection between the flow next to the side wall and that behind the rear wall. A new saddle point S_1 is eventually generated to divide foci F_1 and F_3, as shown in figure 25(*c*). The secondary separation and consequent small-scale vortices in turn alter the flow topology on the walls of the cylinder. For example, the attachment lines form near the leading and trailing edges on the side walls. The same holds true for the flow above the top wall. In particular, the trailing-edge vortices may induce a very sharp drop of pressure instantaneously (Tambara *et al.* 2018), which may not be observed in the low-*Re* flows when the trailing-edge vortex is absent. The clarification of trailing-edge vortex should aid the flow control methods (Choi, Jeon & Kim 2008; Chen *et al.* 2015*a*,*b*) to reduce localized peak suction.

Small-scale motions can also be observed at a high *Re* in the junction region between the cylinder and surface (see foci F_2, F_3 and F_4 in figure 17). This mechanism is similar to the increased number of small-scale vortices in the lid-driven cavity with an increase in the *Re* (Ghia, Ghia & Shin 1982; Wahba 2012).

8. Conclusions

The complete near-wall flow patterns around a surface-mounted square cylinder immersed in a thick turbulent boundary layer at high *Re* values were topologically described for the first time. Small-scale flow separations were captured through a numerical simulation with a very high-resolution Cartesian grid (512×512 cells for an area of $1D \times 1D$). The strict methodology for topological description (i.e. the critical-point concept) was applied to construct rational and consistent flow topologies from bottom to top. A detailed flow topology is considered a valuable database for this fundamental flow geometry. Detailed new findings on the topological description can be summarised as follows.

First, the large-scale near-wake (or arch-type) vortex often observed in the recirculation zone behind the cylinder was composed of two connected segments rolled up from the sides of the cylinder and from the free end. The near-wake vortex was rooted on the two foci behind the cylinder on the ground plane.

Second, another large-scale side vortex occurred at a high *Re*, which could be seen next to the side walls in the horizontal cross-sections or above the top wall in the symmetry plane. Note that the side vortex has not been widely emphasised in the literature because of the absence or incompleteness of the near-wall data. This study found that the side vortex rooted on two notable foci on both side walls of the junction influence region and grew continuously throughout the height of the cylinder. Finally, the side vortex on the two sides of the cylinder was connected above the top wall. The side vortex was also characterised by quantitative variation in the vertical direction. In the junction influence region, the side vortex moved upwards with a curved trajectory instead of in the straight vertical direction. The curved trajectory of the side vortex could be explained by the downward inclination of the separated main flow on the two sides in the junction influence region. The formation of a curved trajectory in the junction region was also believed to be influenced by the squeeze effect of the flow reattachment on the trailing portion of the side walls. Because of the curved trajectory in the junction region, two separation nodes were observed in the surface flow of the ground plane (i.e. N_4 in figure 7*c*). In the free-end influence region, the side vortex was compressed near the side edge of the top wall. The compression contributed to the basic flow type on the top and side walls in the free-end region. In particular, the compression resulted in downstream movement and a smaller trailing-edge vortex in the free-end region.

Only tip vortices were observed in the far wake, which indicated the dipole wake model. Based on the very thick boundary layer and high *Re*, the vorticity of the tip vortex was found to stem from the shear-dominant region above the top wall and next to the side walls of the cylinder. The lateral and vertical vorticities were gradually distorted and stretched to the streamwise vorticity of the tip vortex, which was caused by the difference in the downwash strength and convective velocity between the central and lateral wakes. The relationship between the tip and near-wake vortices was also discussed. The vorticity of the tip vortex originated from the outer region of the shear-dominated separated flow, whereas that of the near-wake vortex originated from the inner region. Moreover, the streamwise vorticity in the near wake was found to be the projected near-wake vortex (instead of the tip vortex), which inclined towards the free end of the cylinder.

A relatively complete topological description has often been studied in the range of low *Re* values ($Re \leq 1000$). This study further clarified the effects of *Re* values by comparing the flow topologies at low and high *Re*. (1) A much shorter recirculation region was observed at the present high *Re*. (2) After carefully surveying the boundary layer thicknesses and *Re* values, we argued that, in addition to the quantitative influence of the boundary layer thickness on the upwash strength (Wang *et al.* 2006), the increase in *Re* from 500 to $O(10^4)$ played a dominant role in the generation of upwash flow in the near and moderate wakes. The mechanism was provided for the presence of upwash at high $Re = O(10^4)$ but absence at low $Re = 500$ and 1000. (3) In comparison with the full separation at low *Re*, the separation–reattachment process was observed in the junction region at a high *Re*. The reattachment at a high *Re* strengthened the inverted conical vortex (i.e. side vortex in the junction region). Thus, this study suggests that the strength of a inverted conical vortex should not ignore the effects derived from the *Re*. (4) Finally, numerous small-scale flow vortices were found to form only at high *Re* values, such as *SSVs* downstream of leading edges, trailing-edge vortices and edge vortices. In particular, the trailing-edge vortex, which is related to the sharp drop in pressure near the trailing edge (Tambara *et al.* 2018), was observed only at a high *Re*. This suggests that the *Re* independence of the local pressures may not be true.

Acknowledgements. The authors are extremely grateful to Dr K. Onishi, Dr R. Bale and Professor M. Tsubokura for their technical support and fruitful discussions regarding the numerical methods, and to Dr H. Kawai for assistance with turbulent inflow generation. The authors also thank the anonymous reviewers for greatly improving the quality of the manuscript.

Funding. The study was funded by the MEXT project: 'Advancement of meteorological and global environmental predictions utilizing observational 'Big Data' of the social and scientific priority issues (Theme 4) to be tackled by using post-K computer of the FLAGSHIP2020 Project' (hp160229, hp170246, hp180194, hp190156), Shanghai Sailing Program (21YF1419400), Natural Science Foundation of Shanghai (21ZR1428900), National Natural Science Foundation of China (52108462, 42076210 and 51879160), Innovation Program of Shanghai Municipal Education Commission (2019-01-07-00-02-E00066) and Oceanic Interdisciplinary Program of Shanghai Jiao Tong University (SL2020PT201).

Declaration of interests. The authors report no conflict of interest.

Author ORCIDs.
Yong Cao https://orcid.org/0000-0002-0262-8251.

Appendix A. Computational domain and cell sizes

A sufficiently large computational domain size is desirable to avoid blockage effects. The effects of domain size in the lateral direction have been systematically studied by the wind engineering community in Japan. The lateral size was suggested to be greater than 10D (AIJ 2017). The present lateral size (8D) is slightly smaller than the recommended value because of the limited lateral width in the data of the turbulent boundary layer which were generated in another in-house code. The possible effects are examined by comparing the present flow field and the results obtained in the larger domain size or in the experiments. It was found that the mean lateral velocity and r.m.s. velocity are very close to zero at the location of the lateral boundaries (i.e. $y/D = 4$ and -4) in the wake of $x/D < 5$. As in the present study, the turbulence intensity or the normalised r.m.s. velocity was reported to be 1 %–2 % in the experimental and DNS results (Saeedi *et al.* 2014; Sohankar *et al.* 2018) at the same location of $y/D = 4$ and $x/D = 5$. This indicates that the flow near the side boundaries is relatively stable (i.e. without significant fluctuations). In the very far wake of $x/D > 5$, the width of the region with high fluctuations becomes increasingly wider (Saeedi *et al.* 2014; Sohankar *et al.* 2018). Thus, the blockage effects become greater in the very far wake and are expected to decrease slightly the rate of growth of the far wake and fluctuation-related quantities. However, no significant influences are expected on the qualitative and quantitative fields in the regions around the cylinder and in the near and moderate wakes, which are the focus of this study. To confirm this conjecture, the profiles of the mean streamwise velocity along the lateral direction are plotted for $z/D = 1.0$, 1.5 and 2.0, as shown in figure 26. The streamwise region is $x/D = 0.6$–3.1. The examination region covers the near and moderate wake regions. The mean velocity in the lateral region of $y/D = 2$–4 remains nearly constant and close to the approaching velocity. This provides more confidence in the conclusion that the near- and moderate-wake flows do not significantly vary by the present lateral distance of the computational domain. The set-up of a large vertical height of the domain size (32D) considers two factors: (i) the top boundary should not influence the separated flow above the top wall of the surface-mounted cylinder, which is suggested to be greater than H above the top wall of the cylinder; and (ii) the height should be sufficiently large to allow the streamwise development of the turbulent boundary layer. In this study, the thickness of the boundary layer is high ($\delta/D = 20.1$) to mimic the atmospheric boundary layer. Therefore, the height of the domain is selected as 32D, which is greater than the boundary layer thickness. The constant free-stream velocity could be set above the top of the boundary layer, which is implemented in the code more easily than the extension of the turbulent boundary layer in the lateral direction.

In fluid turbulence, the Kolmogorov length scale is a dynamical parameter in space and time. However, the standard practice is to use the mean field value to represent the typical values of the smallest scales in a given flow. In other words, the Kolmogorov length scale is estimated by $\eta = (\nu^3/\bar{\epsilon})^{1/4}$, where $\bar{\epsilon}$ is the mean dissipation rate of the turbulent kinetic energy per unit mass: $\bar{\epsilon} = 2\nu\overline{s_{ij}s_{ij}} = \nu\overline{((\partial u_i/\partial x_j)(\partial u_i/\partial x_j) + (\partial u_i/\partial x_j)(\partial u_j/\partial x_i))}$, where s_{ij} is the fluctuating strain rate tensor and u_i is the fluctuating velocity component. Figure 27(*a*) shows the distribution of $\sqrt[3]{V_{cell}}/\eta$ in the region near the cylinder, where V_{cell} is the volume of the cells. The contours are not perfectly smooth because: (i) the statistics are computed using a limited number of output time steps of instantaneous velocity fields (50 time steps evenly); and (ii) the cell sizes vary twice in the transition region of different-scale cubes. Nevertheless, that the contours are not perfectly smooth does not significantly influence the following discussion and conclusions. Figure 27(*b*) plots a histogram of the ratios of cell size to the Kolmogorov scale. The examinations show that

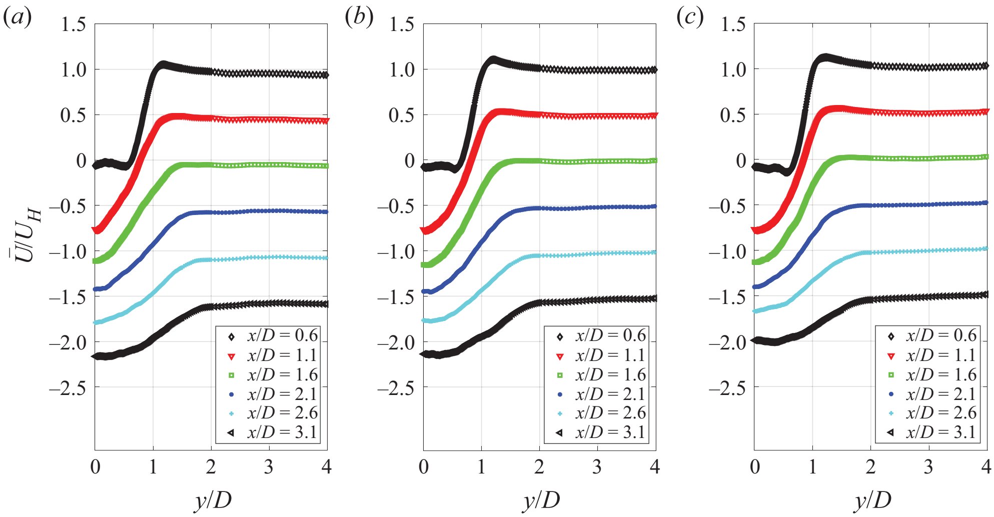

Figure 26. Profiles of mean streamwise velocity along the lateral direction: (*a*) $z/D = 1.0$; (*b*) $z/D = 1.5$; (*c*) $z/D = 2.0$. The profiles are shifted downward by 0.5 for the sake of clarity.

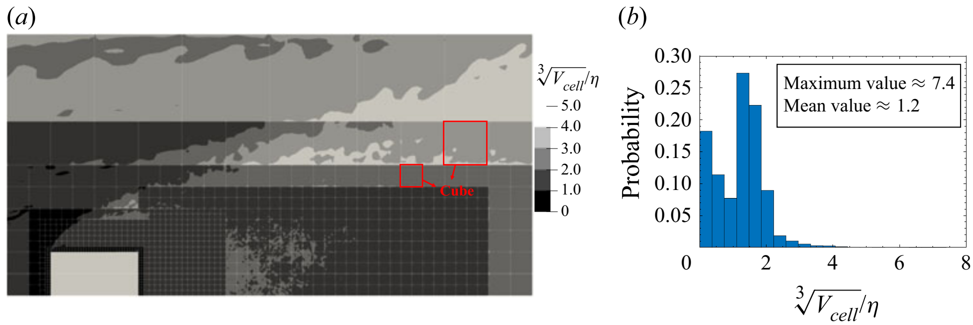

Figure 27. (*a*) Distribution of the ratio between the cube root of cell volume ($\sqrt[3]{V_{cell}}$) and the Kolmogorov length scale (η) in the region of $x/D = [-1, 6]$, $y/D = [0, 3]$ when $z/D = 1.45$. The cube is indicated, which includes $16 \times 16 \times 16$ cells in three directions. (*b*) Histogram of $\sqrt[3]{V_{cell}}/\eta$, where the maximum and mean values are approximately 7.4 and 1.2, respectively.

the maximum and mean values of $\sqrt[3]{V_{cell}}/\eta$ are approximately 7.4 and 1.2, respectively. Most of the kinematic turbulent energy is dissipated at scales of 10η. Therefore, most previous DNSs used 10η as the criteria for determining the appropriate grid resolution. To conclude, the present resolutions are sufficient in comparison with the Kolmogorov length scale.

Appendix B. Temporal convergence of statistical analyses

The duration of the statistical average is approximately $200t^*$, which begins the instant the flow becomes statistically stationary. The statistical pressures and forces converge over the current duration (Cao *et al.* 2019). In this study, the temporal convergence of the direction of wall shear stress and the velocity component in the wake are examined while focusing on the topology of the near-wall and near-wake flows. Similar to the manner of pressure and

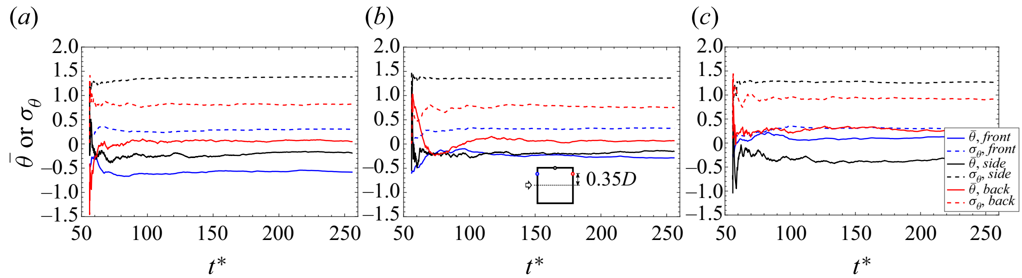

Figure 28. Temporal convergence of the mean and r.m.s. values of the direction of wall shear stress (denoted by θ) at the cross-section: (*a*) $z/D = 0.40$; (*b*) $z/D = 1.45$; (*c*) $z/D = 2.50$.

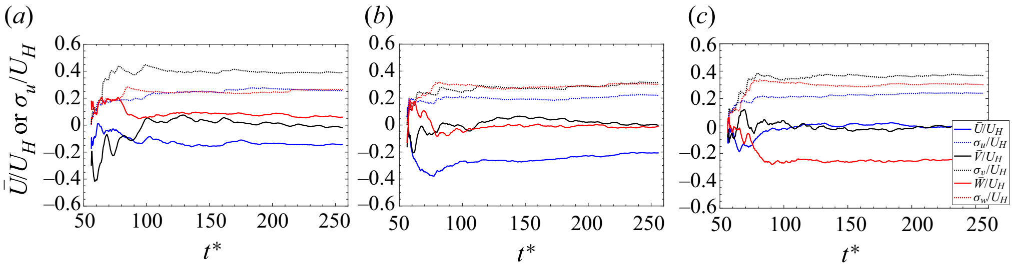

Figure 29. Temporal convergence of the mean and r.m.s. values of velocity components in the near wake when $x/D = 1.5$: (*a*) $z/D = 0.51$; (*b*) $z/D = 1.50$; (*c*) $z/D = 2.50$.

force, the temporal convergence of the mean and r.m.s. values of the direction of wall shear stress θ is examined in figure 28. The direction of the wall shear stress is defined as $\theta = \mathrm{actan}(\tau_{w2}/\tau_{w1})$. Depending on the probe points, we selected three typical points on the frontal, side and back walls when $z/D = 0.40$, 1.45 and 2.50, as indicated in figure 28(*b*). In the case of figure 28, τ_{w2} is the vertical component of the wall shear stress, τ_{w1} is the component along the lateral direction for the frontal and back walls of the cylinder, and τ_{w1} is the component along the streamwise direction of the side wall. It can be clearly seen that the wall shear stress direction converged temporally well until the end of the simulations. No significant changes were expected, even though the simulations continued for a longer duration. Notably, we also checked other probe points along the circumferential direction of the cylinder and the same conclusions of temporal convergence could be drawn. For the near wake, we also checked the temporal convergence of the velocity components when $x/D = 1.5$ and z/D varied between 0.51, 1.50 and 2.50. These are shown in figure 29. Good temporal convergence was achieved for both the mean and r.m.s. values of the three velocity components.

Appendix C. Evaluation of estimation method of skin-friction lines

The skin-friction lines based on the wall shear stress (or the dimensionless form known as skin friction) have a clear physical definition and should be used as much as possible. The wall shear stress can be estimated using the velocity derivative method. This study uses a one-sided two-point finite difference to estimate the skin friction. Hereafter, we examine the influences of the discretisation schemes of the velocity derivative on the direction of the skin-friction lines. The wall shear stress vector on a surface (x_1, x_2) is denoted by (τ_{w1} and τ_{w2}), which are the components parallel to x_1 and x_2, respectively.

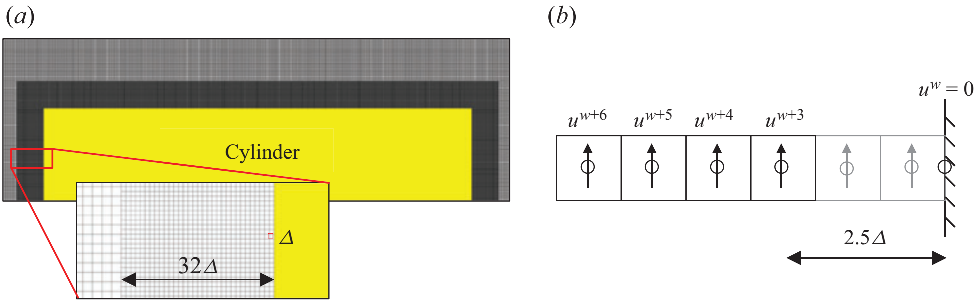

Figure 30. (*a*) Cell distribution near the immersed boundary; (*b*) finite-difference stencil of velocity derivative.

The velocity components along x_1 and x_2 are represented by u and v, respectively. Here, x_3 is the coordinate directed out of the surface (x_1, x_2). The definitions of the wall shear stress are given in (C1) and (C2), where μ is the dynamic viscosity:

$$\tau_{w1} = \mu \left(\frac{\partial u}{\partial x_3} \right)_{x_3=0}, \tag{C1}$$

$$\tau_{w2} = \mu \left(\frac{\partial v}{\partial x_3} \right)_{x_3=0}. \tag{C2}$$

To approximate the velocity derivative on the wall, the one-sided finite difference in the wall-normal direction is tested using a uniform grid. In the present BCM method, the cells (32 total cells) are uniformly distributed near the immersed boundary, as shown in figure 30(*a*). The cell size is Δ in the three directions. Polynomial interpolation is used to construct the discrete form of the velocity derivative. The numerical treatment of the immersed boundary behaves like a velocity damping nearest the boundary. After a private discussion with the authors of Onishi *et al.* (2018), the velocities to be used for physical interpretation were selected from the third cell from the no-slip wall (i.e. u^{w+3}), as shown in figure 30(*b*). Note that u^{w+3} is located at the cell centre away from the wall by 2.5Δ. The velocity on the wall is zero (i.e. $u^w = v^w = 0$).

The wall shear stress is estimated by the following schemes with different orders of accuracy: one-sided two-point; three-point; four-point and five-point stencils. The discrete forms are shown in (C3)–(C6), where τ_{w1} represents the planar component on the wall along the direction of u. The other planar component of the wall shear stress τ_{w2} can be obtained in a straightforward manner by replacing u with v throughout (C3)–(C6).

(i) Two-point stencil, first-order accurate,

$$\tau_{w1}/\mu = \frac{2}{5\Delta} u^{w+3}. \tag{C3}$$

(ii) Three-point stencil, second-order accurate,

$$\tau_{w1}/\mu = \frac{7}{5\Delta} u^{w+3} - \frac{5}{7\Delta} u^{w+4}. \tag{C4}$$

(iii) Four-point stencil, third-order accurate,

$$\tau_{w1}/\mu = \frac{63}{20\Delta} u^{w+3} - \frac{45}{14\Delta} u^{w+4} + \frac{35}{36\Delta} u^{w+5}. \tag{C5}$$

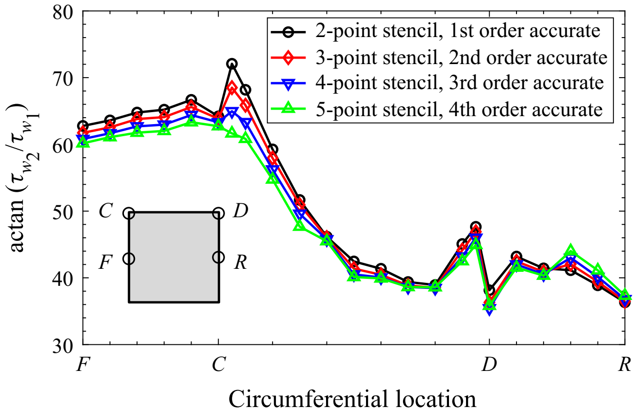

Figure 31. Influence of finite-difference discretisation on the direction of wall shear stress. The cross-section is selected at the middle height of the cylinder.

(iv) Five-point stencil, fourth-order accurate,

$$\tau_{w1}/\mu = \frac{231}{40\Delta}u^{w+3} - \frac{495}{56\Delta}u^{w+4} + \frac{385}{72\Delta}u^{w+5} - \frac{105}{88\Delta}u^{w+6}. \tag{C6}$$

The direction of the wall shear stress is determined by $\arctan(\tau_{w2}/\tau_{w1})$. An examination of the influence of finite-difference accuracy on the direction of wall shear stress is illustrated by the velocity field in the cross-section of the middle height of the cylinder. The results are shown in figure 31 when different numbers of cells are used for estimating the velocity derivative. The curves of $\arctan(\tau_{w2}/\tau_{w1})$ nearly overlap each other, which indicates a small difference between the finite-difference schemes of low- and high-order accuracy. Quantitatively, the maximum disparity among them is approximately 10.4°, and the wall-averaged disparity is approximately 2.8°. The disparity between the finite-difference schemes of low- and high-order accuracy is very small for the direction of the wall shear stress, which is of greater interest for the topological description. To summarise the aforementioned observations, the accuracy order of the finite difference has little influence on the direction of the skin-friction lines. Thus, in this study, using the two-point stencil should be sufficiently accurate for determining and drawing skin-friction lines when focusing on flow topology.

References

AIJ 2017 *Guidebook of Recommendations for Loads on Buildings 2 - Wind-Induced Response and Load Estimation/Practical Guide of CFD for Wind Resistant Design (in Japanese)*. Architectural Institute of Japan.

Bai, H. & Alam, M.M. 2018 Dependence of square cylinder wake on Reynolds number. *Phys. Fluids* **30** (1), 015102.

Baker, C.J. 1979 The laminar horseshoe vortex. *J. Fluid Mech.* **95** (2), 347–367.

Baker, C.J. 1980 The turbulent horseshoe vortex. *J. Wind Engng Ind. Aerodyn.* **6** (1–2), 9–23.

Ballio, F., Bettoni, C. & Franzetti, S. 1998 A survey of time-averaged characteristics of laminar and turbulent horseshoe vortices. *J. Fluids Engng* **120** (2), 233–242.

Behera, S. & Saha, A.K. 2019 Characteristics of the flow past a wall-mounted finite-length square cylinder at low Reynolds number with varying boundary layer thickness. *J. Wind Engng Ind. Aerodyn.* **141** (6), 204–213.

Behera, S. & Saha, A.K. 2021 Effect of inlet shear on turbulent flow past a wall-mounted finite-size square cylinder. *Ocean Engng* **234**, 109270.

BOURGEOIS, J.A., SATTARI, P. & MARTINUZZI, R.J. 2011 Alternating half-loop shedding in the turbulent wake of a finite surface-mounted square cylinder with a thin boundary layer. *Phys. Fluids* **23** (9), 147–542.

CAO, Y. & TAMURA, T. 2015 Numerical investigations into effects of three-dimensional wake patterns on unsteady aerodynamic characteristics of a circular cylinder at $Re = 1.3 \times 10^5$. *J. Fluids Struct.* **59**, 351–369.

CAO, Y. & TAMURA, T. 2016 Large-eddy simulations of flow past a square cylinder using structured and unstructured grids. *Comput. Fluids* **137**, 36–54.

CAO, Y., TAMURA, T. & KAWAI, H. 2019 Investigation of wall pressures and surface flow patterns on a wall-mounted square cylinder using very high-resolution cartesian mesh. *J. Wind Engng Ind. Aerodyn.* **188**, 1–18.

CAO, Y., TAMURA, T. & KAWAI, H. 2020 Spanwise resolution requirements for the simulation of high-Reynolds-number flows past a square cylinder. *Comput. Fluids* **196**, 104320.

CASTRO, I.P. & DIANAT, M. 1983 Surface flow patterns on rectangular bodies in thick boundary layers. *J. Wind Engng Ind. Aerodyn.* **11** (1-3), 107–119.

CHEN, W.L., CAO, Y., LI, H. & HU, H. 2015*a* Numerical investigation of steady suction control of flow around a circular cylinder. *J. Fluids Struct.* **59**, 22–36.

CHEN, W.L., GAO, D.L., YUAN, W.Y., LI, H. & HU, H. 2015*b* Passive jet control of flow around a circular cylinder. *Exp. Fluids* **56** (11), 201.

CHOI, H., JEON, W.P. & KIM, J. 2008 Control of flow over a bluff body. *Annu. Rev. Fluid Mech.* **40**, 113–139.

CHONG, M.S., PERRY, A.E. & CANTWELL, B.J. 1990 A general classification of three-dimensional flow fields. *Phys. Fluids* A*: Fluid Dyn.* **2** (5), 765–777.

DALLMANN, U. 1983 Topological structures of three-dimensional vortex flow separation. *AIAA Paper* 1983-1735.

DALLMANN, U. & SCHEWE, G. 1987 On topological changes of separating flow structures at transition Reynolds numbers. *AIAA Paper* 1987-1266.

DAVEY, A. 1961 Boundary-layer flow at a saddle point of attachment. *J. Fluid Mech.* **10** (4), 593–610.

DEPARDON, S., LASSERRE, J.J., BOUEILH, J.C., BRIZZI, L.E. & BORÉE, J. 2005 Skin friction pattern analysis using near-wall PIV. *Exp. Fluids* **39** (5), 805–818.

DÉLERY, J.M. 2001 Robert legendre and Henri Werlé: toward the elucidation of three-dimensional separation. *Annu. Rev. Fluid Mech.* **33**, 129–154.

DÉLERY, J.M. 2013 *Three-Dimensional Separated Flow Topology: Critical Points, Separation Lines and Vortical Structures*. John Wiley & Sons.

DOUSSET, V. & POTHÉRAT, A. 2010 Formation mechanism of hairpin vortices in the wake of a truncated square cylinder in a duct. *J. Fluid Mech.* **653**, 519–536.

ESCAURIAZA, C. & SOTIROPOULOS, F. 2011 Reynolds number effects on the coherent dynamics of the turbulent horseshoe vortex system. *Flow Turbul. Combust.* **86** (2), 231–262.

GHIA, U., GHIA, K.N. & SHIN, C.T. 1982 High-re solutions for incompressible flow using the Navier–Stokes equations and a multigrid method. *J. Comput. Phys.* **48** (3), 387–411.

HOSSEINI, Z., BOURGEOIS, J.A. & MARTINUZZI, R.J. 2013 Large-scale structures in dipole and quadrupole wakes of a wall-mounted finite rectangular cylinder. *Exp. Fluids* **54** (9), 1595.

HUANG, R.F., CHEN, J.M. & HSU, C.M. 2006 Modulation of surface flow and vortex shedding of a circular cylinder in the subcritical regime by a self-excited vibrating rod. *J. Fluid Mech.* **555**, 321–352.

HUANG, R.F., LIN, B.H. & YEN, S.C. 2010 Time-averaged topological flow patterns and their influence on vortex shedding of a square cylinder in crossflow at incidence. *J. Fluids Struct.* **26** (3), 406–429.

HUNT, J.C.R., ABELL, C.J., PETERKA, J.A. & WOO, H. 1978 Kinematical studies of the flows around free or surface-mounted obstacles; applying topology to flow visualization. *J. Fluid Mech.* **86** (01), 179–200.

JANSSON, N., BALE, R., ONISHI, K. & TSUBOKURA, M. 2019 Cube: a scalable framework for large-scale industrial simulations. *Intl J. High Performance Comput. Appl.* **33** (4), 678–698.

JIANG, H. & CHENG, L. 2018 Hydrodynamic characteristics of flow past a square cylinder at moderate Reynolds numbers. *Phys. Fluids* **30** (10), 104107.

JIANG, H. & CHENG, L. 2020 Flow separation around a square cylinder at low to moderate Reynolds numbers. *Phys. Fluids* **32** (4), 044103.

JIANG, H., CHENG, L. & AN, H. 2018 Three-dimensional wake transition of a square cylinder. *J. Fluid Mech.* **842**, 102–127.

KAWAI, H., OKUDA, Y. & OHASHI, M. 2012 Near wake structure behind a 3d square prism with the aspect ratio of 2.7 in a shallow boundary layer flow. *J. Wind Engng Ind. Aerodyn.* **104**, 196–202.

KAWAMURA, T., HIWADA, M., HIBINO, T., MABUCHI, I. & KUMADA, M. 1984 Flow around a finite circular cylinder on a flat plate: cylinder height greater than turbulent boundary layer thickness. *Bull. JSME* **27** (232), 2142–2151.

Le Clainche, S., Rodriguez, D., Theofilis, V. & Soria, J. 2016 Formation of three-dimensional structures in the hemisphere-cylinder. *AIAA J.* **54** (12), 1–11.

Lee, B.E. 1975 The effect of turbulence on the surface pressure field of a square prism. *J. Fluid Mech.* **69** (2), 263–282.

Legendre, R. 1956 Separation de l'ecoulement laminaire tridimensio-nell. *La Rech. Aéronaut.* **54**, 3–8.

Legendre, R. 1965 Lignes de courant dun ecoulement continu. *Rech. Aerosp.* **105**, 3–9.

Liakos, A. & Malamataris, N.A. 2014 Direct numerical simulation of steady state, three dimensional, laminar flow around a wall mounted cube. *Phys. Fluids* **26** (5), 053603.

Liakos, A. & Malamataris, N.A. 2016 Three-dimensional, laminar flow past a short, surface-mounted cylinder. *AIAA J.* **54** (8), 2310–2321.

Lighthill, M.J. 1963 Attachment and separation in three-dimensional flows. In *Laminar boundary layers theory*, Sect. 927 II2.6 (ed. L. Rosenhead), pp. 72–82. Oxford University Press.

Lund, T.S., Wu, X. & Squires, K.D. 1998 Generation of turbulent inflow data for spatially-developing boundary layer simulations. *J. Comput. Phys.* **140** (2), 233–258.

Markowski, P., Richardson, Y., Rasmussen, E., Straka, J., Davies-Jones, R. & Trapp, R.J. 2008 Vortex lines within low-level mesocyclones obtained from pseudo-dual-doppler radar observations. *Mon. Weath. Rev.* **136** (9), 3513–3535.

Martinuzzi, R. & Tropea, C. 1993 The flow around surface-mounted, prismatic obstacles placed in a fully developed channel flow (data bank contribution). *J. Fluids Engng* **11** (1), 85–92.

Maruyama, Y., Tamura, T., Okuda, Y. & Ohashi, M. 2013 LES of fluctuating wind pressure on a 3D square cylinder for PIV-based inflow turbulence. *J. Wind Engng Ind. Aerodyn.* **122**, 130–137.

Maskell, E.C. 1955 Flow separation in three dimensions. R.A.E. Rep. Aero. no. 2565.

Mcclean, J.F. & Sumner, D. 2014 An experimental investigation of aspect ratio and incidence angle effects for the flow around surface-mounted finite-height square prisms. *J. Fluids Engng* **136** (8), 081206.

Nakahashi, K. 2002 Building-cube method for flow problems with broadband characteristic length. In *Proceedings of the ICCFD2, Computational Fluid Dynamics 2002*, pp. 77–81.

Nakahashi, K. 2005 High-density mesh flow computations with pre-/post-data compressions. In *AIAA Computational Fluid Dynamics Conference. AIAA Paper* 2005-4876.

Noda, H. & Nakayama, A. 2003 Free-stream turbulence effects on the instantaneous pressure and forces on cylinders of rectangular cross section. *Exp. Fluids* **34** (3), 332–344.

Nozawa, K. & Tamura, T. 2002 Large eddy simulation of the flow around a low-rise building immersed in a rough-wall turbulent boundary layer. *J. Wind Engng Ind. Aerodyn.* **90** (10), 1151–1162.

Nozu, T. & Tamura, T. 2012 Les of turbulent wind and gas dispersion in a city. *J. Wind Engng Ind. Aerodyn.* **104**, 492–499.

Okuda, Y. & Taniike, Y. 1993 Conical vortices over side face of a three-dimensional square prism. *J. Wind Engng Ind. Aerodyn.* **50**, 163–172.

Ong, L. & Wallace, J. 1996 The velocity field of the turbulent very near wake of a circular cylinder. *Exp. Fluids* **20** (6), 441–453.

Onishi, K., Ando, Y., Nakasato, K. & Tsubokura, M. 2018 Evaluation of an open-grill vehicle aerodynamics simulation method considering dirty cad geometries. *SAE Technical Paper* (2018-01-0733).

Onishi, K., Obayashi, S., Nakahashi, K. & Tsubokura, M. 2013 Use of the immersed boundary method within the building cube method and its application to real vehicle CAD data. In *21st AIAA Computational Fluid Dynamics Conference. AIAA Paper* 2013-2713.

Onishi, K. & Tsubokura, M. 2021 Topology-free immersed boundary method for incompressible turbulence flows: an aerodynamic simulation for 'dirty' cad geometry. *Comput. Meth. Appl. Mech. Engng* **378**, 113734.

Oswatitsch, K. 1958 Die Ablösungsbedingung von Grenzschichten. In *Grenzschichtforschung* (ed. H. Goertler). Springer-Verlag.

van Oudheusden, B.W., Scarano, F., van Hinsberg, N.P. & Roosenboom, E.W.M. 2008 Quantitative visualization of the flow around a square-section cylinder at incidence. *J. Wind Engng Ind. Aerodyn.* **96** (6-7), 913–922.

Parnaudeau, P., Carlier, J., Heitz, D. & Lamballais, E. 2008 Experimental and numerical studies of the flow over a circular cylinder at Reynolds number 3900. *Phys. Fluids* **20** (8), 085101.

Perry, A.E. & Chong, M.S. 1987 A description of eddying motions and flow patterns using critical-point concepts. *Annu. Rev. Fluid Mech.* **19** (1), 125–155.

Poincaré, H. 1891 Les points singuliers des Équations differéntielles. In *Œuvres Complétes*, vol. 1, pp. 125–155. Comptes-Rendus de l'Académie des Science.

PORTEOUS, R., MOREAU, D.J. & DOOLAN, C.J. 2016 The aeroacoustics of finite wall-mounted square cylinders. *J. Fluid Mech.* **832**, 287–328.

RASTAN, M.R., SHAHBAZI, H., SOHANKAR, A., ALAM, M.M. & ZHOU, Y. 2021 The wake of a wall-mounted rectangular cylinder: cross-sectional aspect ratio effect. *J. Wind Engng Ind. Aerodyn.* **213**, 104615.

RASTAN, M.R., SOHANKAR, A. & ALAM, M.M. 2017 Low-Reynolds-number flow around a wall-mounted square cylinder: flow structures and onset of vortex shedding. *Phys. Fluids* **29** (10), 103601.

RASTAN, M.R., SOHANKAR, A., DOOLAN, C., MOREAU, D., SHIRANI, E. & ALAM, M.M. 2019 Controlled flow over a finite square cylinder using suction and blowing. *Intl J. Mech. Sci.* **156**, 410–434.

SAEEDI, M., LEPOUDRE, P.P. & WANG, B.C. 2014 Direct numerical simulation of turbulent wake behind a surface-mounted square cylinder. *J. Fluids Struct.* **51**, 20–39.

SAHA, A.K. 2013 Unsteady flow past a finite square cylinder mounted on a wall at low Reynolds number. *Comput. Fluids* **88**, 599–615.

SAKAMOTO, H. & ARIE, M. 1983 Vortex shedding from a rectangular prism and a circular cylinder placed vertically in a turbulent boundary layer. *J. Fluid Mech.* **126**, 147–165.

DA SILVA, B.L., CHAKRAVARTY, R., SUMNER, D. & BERGSTROM, D.J. 2020 Aerodynamic forces and three-dimensional flow structures in the mean wake of a surface-mounted finite-height square prism. *Intl J. Heat Fluid Flow* **83**, 108569.

SOHANKAR, A., ESFEH, M.K., POURJAFARI, H., ALAM, M.M. & WANG, L. 2018 Features of the flow over a finite length square prism on a wall at various incidence angles. *Wind Struct.* **26** (5), 317–329.

SUJUDI, D. & HAIMES, R. 1995 Identification of swirling flow in 3-D vector fields. In *AIAA 12th Computational Fluid Dynamics Conference. AIAA Paper* 1995-1715.

SUMNER, D. 2013 Flow above the free end of a surface-mounted finite-height circular cylinder: a review. *J. Fluids Struct.* **43**, 41–63.

SUMNER, D., ROSTAMY, N., BERGSTROM, D.J. & BUGG, J.D. 2017 Influence of aspect ratio on the mean flow field of a surface-mounted finite-height square prism. *Intl J. Heat Fluid Flow* **65**, 1–20.

TAMBARA, C., ONO, Y., IIDA, Y. & TAMRUA, T. 2018 Study on characteristics of local suction and evaluation of peak wind pressure coefficients of a three-dimensional square cylinder based on les high-resolution computations. In *Proceedings of 25th National Symposium on Wind Engineering*, pp. 229–234.

TAO, T. & TAMURA, T. 2020 Numerical study of the 6 May 2012 Tsukuba supercell tornado: vorticity sources responsible for tornadogenesis. *Mon. Weath. Rev.* **148** (3), 1205–1228.

TENNEKES, H. & LUMLEY, J.L. 1972 *A First Course in Turbulence*. MIT Press.

TIAN, Q., SIMPSON, R.L. & TANG, G. 2004 Flow visualization on the linear compressor cascade endwall using oil flows and laser doppler anemometry. *Meas. Sci. Technol.* **15** (9), 1910–1916.

TOBAK, M. & PEAKE, D.J. 1982 Topology of three-dimensional separated flows. *Annu. Rev. Fluid Mech.* **14** (1), 61–85.

TRIAS, F., GOROBETS, A. & OLIVA, A. 2015 Turbulent flow around a square cylinder at Reynolds number 22,000: a DNS study. *Comput. Fluids* **123**, 87–98.

UFFINGER, T., ALI, I. & BECKER, S. 2013 Experimental and numerical investigations of the flow around three different wall-mounted cylinder geometries of finite length. *J. Wind Engng Ind. Aerodyn.* **119**, 13–27.

UNNIKRISHNAN, S., OGUNREMI, A. & SUMNER, D. 2017 The effect of incidence angle on the mean wake of surface-mounted finite-height square prisms. *Intl J. Heat Fluid Flow* **66**, 137–156.

WAHBA, E.M. 2012 Steady flow simulations inside a driven cavity up to Reynolds number 35 000. *Comput. Fluids* **66**, 85–97.

WANG, H., ZHAO, X., HE, X. & ZHOU, Y. 2017 Effects of oncoming flow conditions on the aerodynamic forces on a cantilevered square cylinder. *J. Fluids Struct.* **75**, 140–157.

WANG, H.F. & ZHOU, Y. 2009 The finite-length square cylinder near wake. *J. Fluid Mech.* **638**, 453–490.

WANG, H.F., ZHOU, Y., CHAN, C.K. & LAM, K.S. 2006 Effect of initial conditions on interaction between a boundary layer and a wall-mounted finite-length-cylinder wake. *Phys. Fluids* **18** (6), 065106.

WANG, Y., THOMPSON, D. & HU, Z. 2019 Effect of wall proximity on the flow over a cube and the implications for the noise emitted. *Phys. Fluids* **31** (7), 077101.

WHITE, F.M. 2006 *Viscous Fluid Flow*. Mcgraw Hill.

YAUWENAS, Y., PORTEOUS, R., MOREAU, D.J. & DOOLAN, C.J. 2019 The effect of aspect ratio on the wake structure of finite wall-mounted square cylinders. *J. Fluid Mech.* **875**, 929–960.

ZHANG, D., CHENG, L., AN, H. & ZHAO, M. 2017 Direct numerical simulation of flow around a surface-mounted finite square cylinder at low Reynolds numbers. *Phys. Fluids* **29** (4), 453–490.

ZHAO, C., WANG, H., ZENG, L., ALAM, M.M. & ZHAO, X. 2021 Effects of oncoming flow turbulence on the near wake and forces of a 3D square cylinder. *J. Wind Engng Ind. Aerodyn.* **214**, 104674.

ZU, G. & LAM, K.M. 2018 Simultaneous measurement of wind velocity field and wind forces on a square tall building. *Adv. Struct. Engng* **21** (15), 2241–2258.